

MOLECULAR BIOLOGY

Light-activated macromolecular phase separation modulates transcription by reconfiguring chromatin interactions

Yoon Jung Kim^{1,2†}, Michael Lee Jr^{1,2†}, Yi-Tsang Lee^{3†}, Ji Jing^{3†}, Jacob T. Sanders^{4‡}, Giovanni A. Botten^{1,2}, Lian He³, Junhua Lyu^{1,2§}, Yuannyu Zhang^{1,2§}, Marcel Mettlen⁵, Peter Ly⁴, Yubin Zhou^{3,6*}, Jian Xu^{1,2§*}

Biomolecular condensates participate in the regulation of gene transcription, yet the relationship between nuclear condensation and transcriptional activation remains elusive. Here, we devised a biotinylated CRISPR-dCas9-based optogenetic method, light-activated macromolecular phase separation (LAMPS), to enable inducible formation, affinity purification, and multiomic dissection of nuclear condensates at the targeted genomic loci. LAMPS-induced condensation at enhancers and promoters activates endogenous gene transcription by chromatin reconfiguration, causing increased chromatin accessibility and de novo formation of long-range chromosomal loops. Proteomic profiling of light-induced condensates by dCas9-mediated affinity purification uncovers multivalent interaction-dependent remodeling of macromolecular composition, resulting in the selective enrichment of transcriptional coactivators and chromatin structure proteins. Our findings support a model whereby the formation of nuclear condensates at native genomic loci reconfigures chromatin architecture and multiprotein assemblies to modulate gene transcription. Hence, LAMPS facilitates mechanistic interrogation of the relationship between nuclear condensation, genome structure, and gene transcription in living cells.

INTRODUCTION

Nucleated condensates formed by macromolecular assemblies or liquid-liquid phase separation are recognized as a fundamental mechanism to explain the biophysical basis of chromatin organization and gene regulation (1–4). The formation of biomolecular condensates is largely driven by multivalent interactions among low-complexity domains (LCDs) or intrinsically disordered regions (IDRs) (5–8), although the molecular principles governing the propensity of biomolecules to phase separate remain incompletely understood. IDR-mediated phase separation has been postulated as a mechanism by which transcription factors (TFs) and coactivators induce gene activation (9–13); however, there remains no direct evidence nor mechanistic details of whether and how nuclear condensates regulate endogenous gene transcription, largely because of a lack of experimental tools for the targeted formation and purification of nucleated condensates at native chromatin.

Advances in optogenetic platforms that use light to activate IDR-mediated macromolecular assemblies have provided crucial insights

into the biophysical properties of inducible condensation, but existing tools rely primarily on the random nucleation of intracellular condensates with limited information about effects on gene transcription or chromatin regulation (14–16). By combining optogenetics with catalytically dead CRISPR-Cas9 (dCas9) or tetO operators, a few improved strategies were developed to examine the effects of condensate formation on chromatin function or gene expression (17, 18); however, these methods preclude simultaneous analyses of chromatin configuration and interactions caused by localized condensation. Moreover, the molecular composition of nuclear condensates, which may provide critical insight into their formation and function in living cells, has not been evaluated.

To address this critical technical gap, we describe here a new approach, termed light-activated macromolecular phase separation or LAMPS, coupling optogenetics with dCas9-mediated chromatin capture to dissect the molecular composition and functional consequences of inducible condensation at native chromatin in living cells. We establish evidence that LAMPS-induced condensation at endogenous enhancers and promoters activates transcription by reconfiguring chromatin accessibility, DNA looping, and multiprotein assemblies. Affinity purification and comparative proteomic profiling of LAMPS-induced condensates yield mechanistic insights into condensation-dependent compartmentalization of higher-order assemblies for gene activation. Our findings support a model in which nuclear condensation regulates gene transcription by selectively reconstituting local macromolecular composition and assembly to reconfigure chromatin structure and function.

¹Children's Medical Center Research Institute, University of Texas Southwestern Medical Center, Dallas, TX 75390, USA. ²Department of Pediatrics, Harold C. Simmons Comprehensive Cancer Center, and Hamon Center for Regenerative Science and Medicine, University of Texas Southwestern Medical Center, Dallas, TX 75390, USA. ³Center for Translational Cancer Research, Institute of Biosciences and Technology, Texas A&M Health Science Center, Houston, TX 77030, USA. ⁴Department of Pathology, University of Texas Southwestern Medical Center, Dallas, TX 75390, USA. ⁵Department of Cell Biology, University of Texas Southwestern Medical Center, Dallas, TX 75390, USA. ⁶Department of Translational Medical Sciences, College of Medicine, Texas A&M University, Houston, TX 77030, USA. *Corresponding author. Email: yubinzhou@tamu.edu (Y. Zhou); jian.xu@utsouthwestern.edu (J.X.)

[†]These authors contributed equally to this work.

[‡]Present address: Department of Biochemistry and Cellular and Molecular Biology, University of Tennessee, Knoxville, TN, USA.

[§]Present address: Center of Excellence for Leukemia Studies (CELS), Department of Pathology, St. Jude Children's Research Hospital, Memphis, TN, USA.

RESULTS

Design of LAMPS

Optogenetic approaches have recently been leveraged to dissect the biophysical properties of biomolecular condensates by fusing the photolyase homology region (PHR) domain of the *Arabidopsis thaliana* cryptochrome 2 (CRY2) (19) to various IDR domains, enabling inducible and reversible condensation in living cells (14–18). When fused to dCas9, light-induced condensates targeted to telomeres preferentially formed across low-density genomic regions, mechanically extruding chromatin into spatially segregated territories akin to chromosomal compartments (17). The nonuniform condensation of genomic regions suggests that biomolecular condensation could generate the biophysical force to shape chromatin architecture such as enhancer-promoter looping for gene activation; however, this hypothesis has not been substantiated by the direct measurement of condensation-mediated effects on gene transcription and chromatin configuration (17, 20). Thus, there remains an unmet need for experimental means to simultaneously induce targeted condensation, assess functional consequences of condensate formation, and dissect their biomolecular composition at native chromatin.

In designing LAMPS, we sought to leverage light-induced condensate formation, dCas9 and single guide RNA (sgRNA)-mediated targeting to a single endogenous genomic locus, and affinity purification to characterize nuclear condensates in situ (Fig. 1A). We first devised a multicistronic construct containing an N-terminal IDR, an mCherry fluorescent reporter, a CRY2-PHR fusion protein, a dCas9 flanked by nuclear localization signals (NLS), and a C-terminal biotin acceptor (BioTAP) recognized by endogenous biotin ligases (Fig. 1B) (21, 22). Upon coexpression of sequence-specific sgRNAs and in vivo biotinylation of dCas9-CRY2-mCherry-IDR fusion proteins in living cells, the genomic locus-associated macromolecules are induced to form condensates by blue light illumination and subsequently isolated by biotin-streptavidin-based high-affinity purification. The purified protein-DNA complexes are identified and characterized by proteomics and chromatin conformation capture (3C) (23) for study of condensation-associated proteins and DNA looping, respectively (Fig. 1A) (21, 22, 24). Hence, LAMPS offers the unique capacity for spatiotemporal control of nuclear condensation with parallel analysis of gene transcription and chromatin regulation, enabling the dissection of the molecular links between nuclear condensation and transcriptional function at endogenous genomic loci.

Activation of endogenous gene transcription by LAMPS-induced condensation

The efficiency of light-activated macromolecule clustering is a critical factor in the design of inducible condensation. We first optimized the blue light-responsive CRY2 module in the LAMPS design. Several CRY2 variants have been described with differing light-activated oligomerization propensities, including a Glu-to-Gly substitution at position 490 of CRY2 (CRY2^{E490G}) (25), a E490R substitution (CRY2^{E490R}) (26), and a variant modified with a C-terminal 9-mer peptide (CRY2^{Clust}) (Fig. 1B) (27). We tested constructs containing wild-type (WT) or variant CRY2 fused to mCherry and dCas9 (fig. S1A) and observed their oligomerization properties. Upon transient expression in HeLa cells followed by flow cytometry sorting of cells based on comparable expression of both

mCherry and zsGreen from dCas9-CRY2 and sgRNA constructs, respectively (fig. S1, B to D), all dCas9-CRY2 constructs exhibited dim and diffuse signals distributed within the nucleoplasm under the nonilluminated (dark) condition. After light illumination for 5 min at 488 nm, mCherry puncta were readily detected (Fig. 1C). Similar puncta formation was observed in cells with or without nontargeting (sgGal4) or sequence-specific sgRNAs (sgHS2), indicating that sgRNA expression has no effect on dCas9-CRY2-mediated condensation. Moreover, dCas9-CRY2^{Clust} consistently produced the largest and brightest puncta, indicating the most robust oligomerization upon light activation (Fig. 1C).

We next determined whether LAMPS-mediated condensate formation at dCas9-targeted genomic loci would affect endogenous gene transcription. In proof-of-principle studies, we chose to target the *HS2* enhancer of the β -globin locus control region (LCR) and the *BCL11A* promoter as two testbed cis-regulatory elements (CREs) (Fig. 1B). The *HS2* enhancer is required for the transcriptional activation of β -like globin genes (e.g., *HBB*) (21), whereas *BCL11A* is a TF that controls developmental hemoglobin switching (28). We reasoned these well-characterized CREs, and the low basal expression of their target genes in HeLa cells would provide ideal testbeds to study gene activation. Last, we considered the incorporation of self-associating IDRs into LAMPS, as these domains are the major determinants of biomolecular condensation through multivalent interactions (1, 20). Two prototypical domains, the N-terminal IDR of the FET (FUS, EWS, and TAF15) family protein FUS (FUS^N) and the C-terminal IDRs of the bromodomain protein BRD4 (BRD4 Δ N), are well-established to undergo condensation (4, 7). We therefore examined the effect of incorporating IDRs into LAMPS-induced condensates on target gene expression.

We engineered constructs with or without FUS^N or BRD4 Δ N and measured gene expression before and after light-induced clustering in cells coexpressing dCas9-CRY2 with or without *HS2* enhancer- or *BCL11A* promoter-targeting sgRNAs (sgHS2 and sgBCL11A), respectively (fig. S1, A and B). While light-induced clustering of dCas9-CRY2 variants without IDRs had variable or no effects on *HBB* and *BCL11A* expression, incorporation of IDRs to dCas9-CRY2^{Clust} consistently produced the most notable gene activation despite comparable expression levels of all dCas9-CRY2 variants (Fig. 1D and fig. S1, C and D). LAMPS-induced gene activation was dependent on the coexpression of enhancer- or promoter-targeting sgRNAs, illustrating an dCas9/sgRNA-mediated on-target effect. Moreover, the IDR-fused dCas9-CRY2^{Clust} consistently displayed larger sizes, higher intensities, and faster kinetics of puncta formation relative to other variants following a single pulse of blue light illumination (fig. S2, A to C). These results demonstrate that light-induced clustering of IDR-containing protein complexes activates endogenous gene transcription at native chromatin. Moreover, CRY2^{Clust} outperforms other variants tested for optogenetic control of nuclear condensation and was selected for the finalized LAMPS design in subsequent studies.

Biophysical properties of LAMPS-activated nuclear condensates

Having established the role of the IDR-containing dCas9-CRY2^{Clust} in gene activation, we next assessed the kinetics and biophysical properties of LAMPS-induced condensation by stably expressing IDR-fused dCas9-CRY2^{Clust} with the CRE-targeting sgRNAs in HeLa cells. Compared to control cells (no IDR) or cells under the

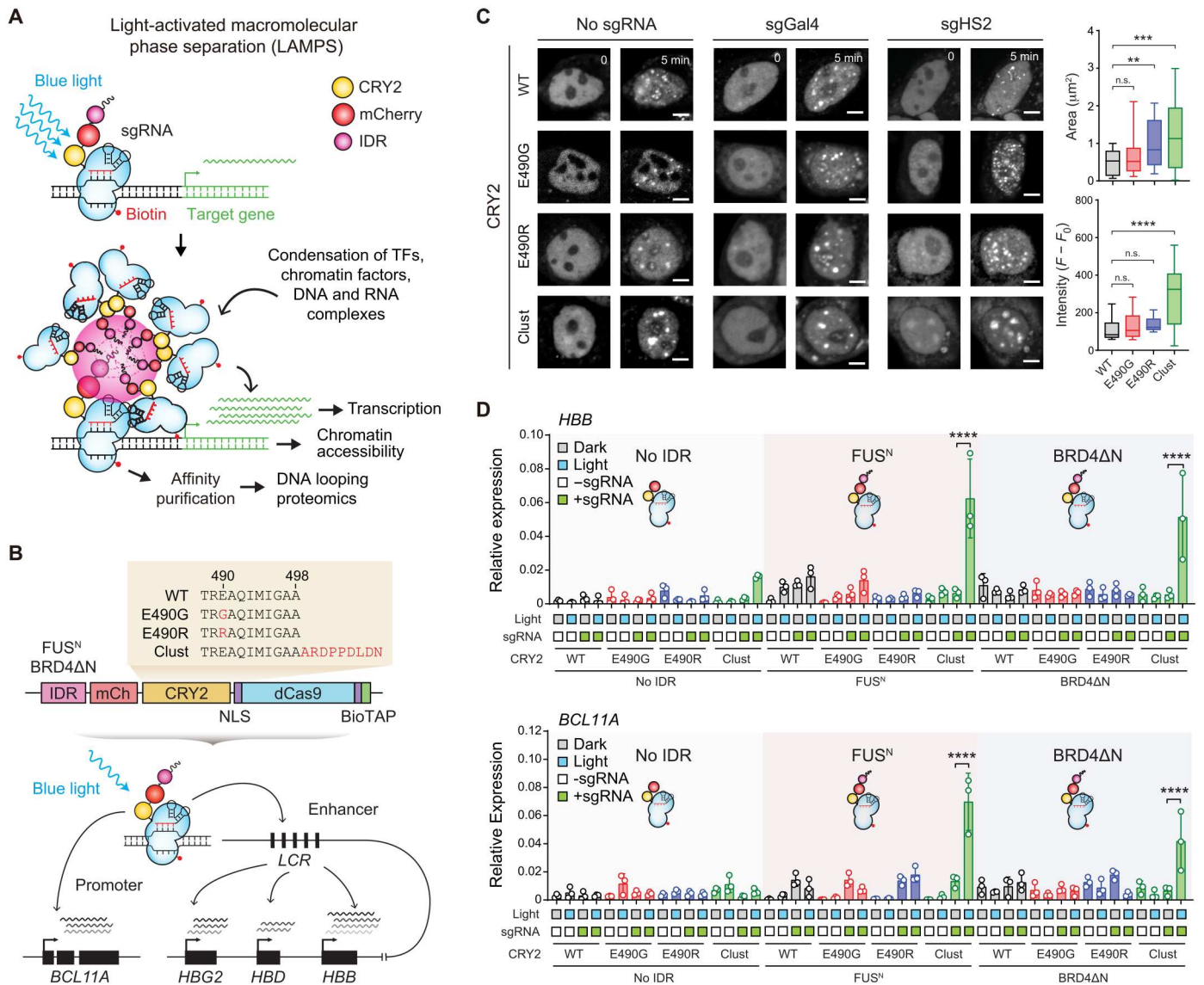


Fig. 1. Development of LAMPS for light-activated nuclear condensation. (A) Schematic of the LAMPS system. LAMPS combines CRY2-based optogenetics with biotinylated dCas9-mediated chromatin capture to dissect the composition and consequences of inducible condensation in gene regulation. (B) Schematic of LAMPS constructs and sgRNA-mediated targeting to the HS2 enhancer and *BCL11A* promoter. Amino acid substitutions for each CRY2 variants relative to WT are highlighted in red. mCh, mCherry; CRY2, CRY2-PHR domain; LCR, locus control region. (C) Representative confocal images are shown for HeLa cells coexpressing dCas9-CRY2 variants without sgRNA (no sgRNA), with nontargeting control (sgGal4) or *HS2*-targeting sgRNA (sgHS2) before and after blue light illumination. Scale bars, 2 μ m. The quantification of areas and changes in intensity by subtracting the initial background signal ($F - F_0$) is shown on the right. The boxes show the median of the data and quartiles, and the whiskers show the minimum and maximum ($N = 27, 27, 26,$ and 22 cells for the quantification of area and $N = 32, 61, 30,$ and 45 cells for the quantification of intensity of dCas9-CRY2 variants without sgRNA). P values were calculated by one-way analysis of variance (ANOVA). $***P < 0.01$, $****P < 0.001$, and $*****P < 0.0001$; n.s., not significant. (D) Analysis of *HBB* and *BCL11A* mRNA expression in HeLa cells transiently coexpressing dCas9-CRY2 variants with or without sgRNAs (sgHS2 and sgBCL11A), IDRs (*FUS*^N and *BRD4* Δ N), and/or blue light illumination (dark and light), respectively. The mRNA expression relative to *GAPDH* is shown. Results are means \pm SD ($N = 3$ independent experiments) and analyzed by one-way ANOVA. P values were calculated by comparing samples under dark and light conditions. $****P < 0.0001$.

dark condition, blue light illumination for 5 min markedly increased *HBB* and *BCL11A* mRNA (11- to 23-fold for *HBB* and 21- to 35-fold for *BCL11A*, respectively; Fig. 2A), consistent with the results of the initial transient overexpression studies (Fig. 1D). By sampling cells at various time points after a single 5-min pulse of illumination, we noted that *HBB* or *BCL11A* mRNA and primary transcripts were progressively and significantly increased over time and peaked at 30 to 45 min after illumination (fig. S3, A and

B). Furthermore, we confirmed that LAMPS condensation could activate target gene expression at other loci including the *MYOD* promoter and *IL1RN* enhancer upon blue light illumination (fig. S3C), indicating that LAMPS-mediated gene activation is generalizable to multiple genomic loci.

To assess the underlying biophysical properties of LAMPS-induced condensation, we performed a series of imaging studies. We noted progressively increased intensities of LAMPS-induced

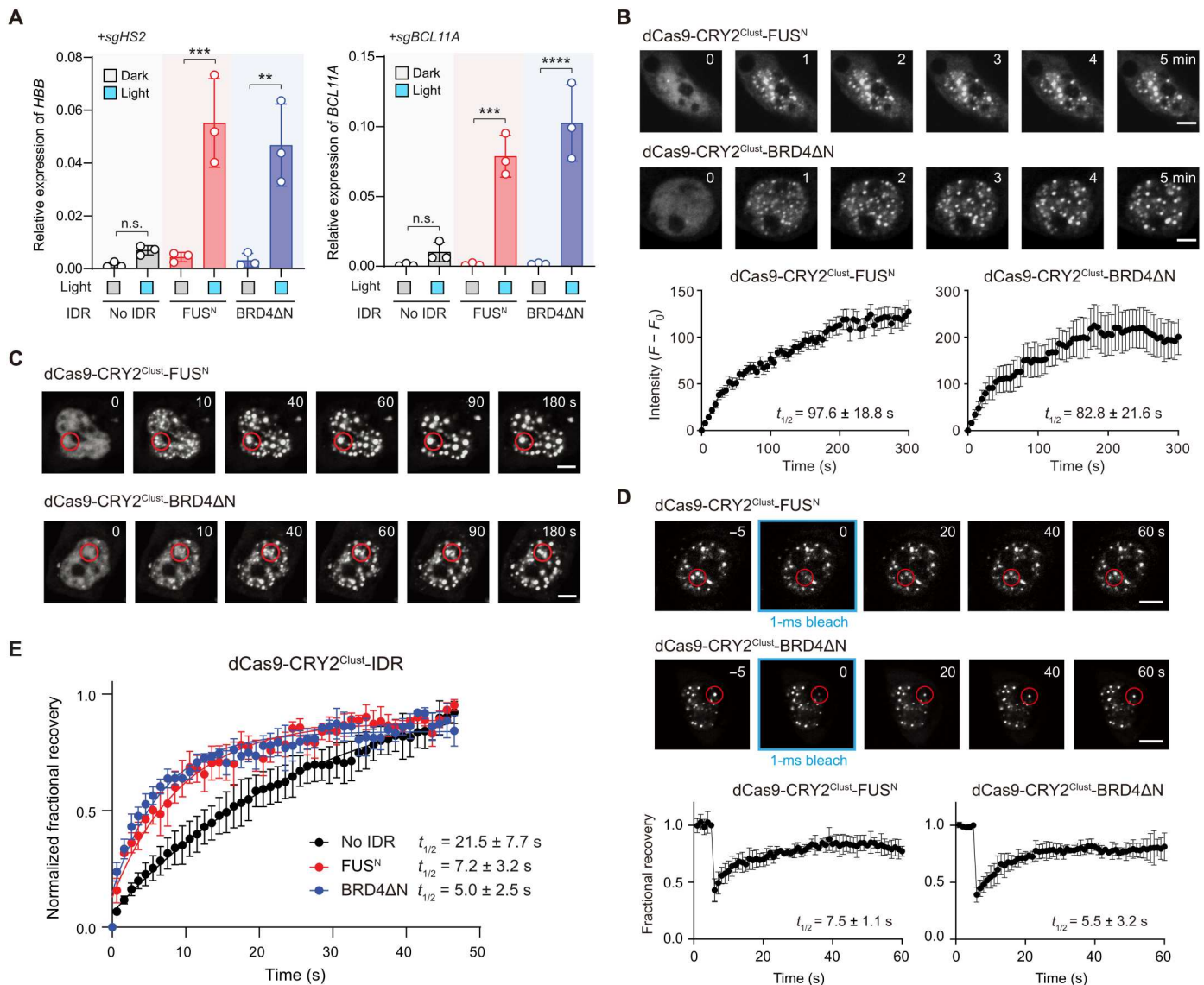


Fig. 2. Properties of LAMPS-induced condensates. (A) Analysis of *HBB* and *BCL11A* mRNA expression in HeLa cells stably coexpressing dCas9-CRY2 variants without (no IDR) or with FUS^N or BRD4ΔN. Results are means \pm SD ($N = 3$ independent experiments) and analyzed by one-way ANOVA. ** $P < 0.01$, *** $P < 0.001$, and **** $P < 0.0001$. (B) Time-lapse confocal images and normalized fluorescence intensities of LAMPS-induced condensates in HeLa stable cells upon blue light illumination. The quantification of normalized fluorescence intensity by subtracting the initial background signal ($F - F_0$) and the half-life ($t_{1/2}$) of maximal intensity are shown. Results are means \pm SEM ($N = 15$ and 12 cells for dCas9-CRY2^{Clust}-FUS^N and dCas9-CRY2^{Clust}-BRD4ΔN, respectively). (C) Representative confocal images are shown for the dynamical fusion of LAMPS-activated condensates (red circles) in HeLa stable cells. Scale bars, 2 μ m. (D) Confocal images are shown for fluorescence recovery after photobleaching (FRAP) assays of LAMPS condensates. The red circles indicate the region bleached by 0.1% laser power for 1 ms, followed by time-lapse confocal imaging to monitor the fluorescence redistribution. The quantification of fractional recovery and the half-life ($t_{1/2}$) are shown. Results are means \pm SD ($N = 3$ and 3 independent experiments for dCas9-CRY2^{Clust}-FUS^N and dCas9-CRY2^{Clust}-BRD4ΔN, respectively). (E) Normalized fractional recovery of HeLa stable cells expressing the indicated LAMPS constructs. The fitting curve of fluorescence recovery (solid line) and the half-life ($t_{1/2}$) of maximum recovery are shown. Results are means \pm SEM ($N = 3$ independent experiments for each LAMPS construct). P values of half-life ($t_{1/2}$) for FUS^N versus no IDR and BRD4ΔN versus no IDR are 0.04 and 0.02, respectively, and were analyzed by unpaired t test.

puncta after blue light illumination with a half-life of puncta formation ($t_{1/2}$) of 97.6 ± 18.8 s and 82.8 ± 21.6 s for dCas9-CRY2^{Clust}-FUS^N and dCas9-CRY2^{Clust}-BRD4ΔN, respectively (Fig. 2B). We next sought evidence to validate whether LAMPS-activated condensates have material properties consistent with membraneless structures in living cells. First, we observed fusion events between distinct puncta upon LAMPS-induced condensation, resulting in their progressive aggregation into larger structures (Fig. 2C), consistent with

liquid-like behavior. Second, we performed fluorescence recovery after photobleaching (FRAP) experiments to determine whether LAMPS-induced puncta are dynamic structures that continually exchange constituent molecules with surrounding partners at steady state, a known property of biomolecular condensates (1–4). Puncta formed by dCas9-CRY2^{Clust}-FUS^N and dCas9-CRY2^{Clust}-BRD4ΔN quickly recovered after localized photobleaching with a half-life of recovery at 7.5 ± 1.1 s and 5.5 ± 3.2 s, respectively (Fig. 2D). Notably,

the puncta formed by dCas9-CRY2^{Clust} without IDR fusion (no IDR) recovered at a slower recovery rate than LAMPS with IDRs (FUS^N or BRD4ΔN) after photobleaching (Fig. 2E), indicating that the presence of IDR potentiates condensate dynamics. Together, these results strongly suggest that LAMPS-activated macromolecule clustering exhibits material properties consistent with biomolecular condensates in living cells.

Molecular determinants of LAMPS-mediated nuclear condensation in living cells

Our tool-building experiments revealed that only the combination of the CRY2^{Clust} variant and IDRs induced puncta formation with notable gene activation (Figs. 1D and 2, A to E), suggesting that IDRs are indispensable for LAMPS-mediated effects on transcription. These findings raised an important question about the molecular determinants of LAMPS-mediated nuclear condensation in living cells. We reasoned that CRY2^{Clust} oligomerization confers LAMPS with sufficient nucleating energy to seed condensates but alone lacks the biophysical and/or biochemical property conferred by IDRs, which is needed to selectively compartmentalize molecules into condensates for gene activation. Consequently, CRY2^{Clust} in this model can potentiate the nucleation of IDR-mediated condensates more than the other CRY2 variants to induce IDR-dependent gene activation.

To test this hypothesis, we leveraged two recently established mutants, one impairing CRY2^{Clust} homo-oligomerization by a Leu-7-Lys (L7K) CRY2^{Clust} mutation (27) and the other abrogating FUS^N-IDR condensation by 15 Tyr-to-Ser substitutions (29). We first tested the CRY2^{Clust} L7K mutant (hereafter Clust^{mut}; Fig. 3A) that alters the hydrophobicity of the C-terminal Clust 9-mer peptide (ARDPPDLN) required for its enhanced homo-clustering compared to WT CRY2 (27). We observed that FUS^N-fused LAMPS condensates harboring Clust^{mut} had reduced kinetics of puncta formation compared to those with native Clust upon blue light illumination (Fig. 3B). Clust^{mut}-induced puncta were also less dynamic, exhibiting slower recovery kinetics after localized photobleaching with a half-life of recovery 10.7 ± 2.7 s compared to 4.6 ± 0.9 s for native Clust (Fig. 3C). These findings suggest that the CRY2 moiety primarily seeds condensate formation, as impairing Clust-driven clustering propensity by point mutation while retaining FUS^N may still endow nascent Clust^{mut} condensates with an IDR-dependent composition that promotes gene activation, although with reduced efficiency due to impaired CRY2 seeding. To test the role of IDRs in condensation dynamics, we incorporated the FUS^N IDR mutant, which contains 15 Tyr-to-Ser substitutions in a critical tract of FUS^N IDR known to impair condensation (hereafter FUS^{Nmut}; Fig. 3A) (29). As expected, FUS^{Nmut} fused to CRY2^{Clust} both impaired light-induced condensate formation and reduced its recovery rate after photobleaching to a greater degree than Clust^{mut}, whereas double mutation of Clust and FUS^N (hereafter FUS^{Nmut}-Clust^{mut}) impaired light-activated condensation to levels comparable to native Clust without IDRs (Figs. 2E and 3, B and C). The dominant effect of FUS^N mutation on condensate dynamics suggests that IDRs may confer permeability to condensates such that constituent molecules are dynamically incorporated.

To test whether and how the modulation of LAMPS condensation by altering clustering efficiency or IDR sequence affects target gene transcription, we measured gene expression in HeLa cells co-expressing WT or mutant LAMPS with *HS2* enhancer-targeting

sgRNAs by transient transfection and in stable cell lines. Notably, Clust^{mut} alone reduced the target gene (*HBB*) expression to 68.9 and 65.8% of the levels induced by native CRY2^{Clust} in both transient and stable expression cells (Fig. 3, D and E). FUS^{Nmut} alone reduced *HBB* expression to 26.9 and 21.1% of the levels induced by WT FUS^N, whereas the FUS^{Nmut}-Clust^{mut} double mutant abolished gene activation (Fig. 3, D and E), suggesting a dominant role of IDRs in LAMPS-mediated gene activation. Together, these findings not only provide insight into distinct functions of LAMPS components (CRY2^{Clust} versus IDR) in controlling condensation-mediated gene activation but also showcase how the modularity of LAMPS components could be broadly leveraged to fine-tune gene activity and dissect the biophysical basis of condensation-dependent gene regulation using programmable condensates.

Targeting of LAMPS-induced condensation to native genomic loci

Transcription-dependent biomolecular condensation emerges as a key feature of gene regulation (9–12, 30, 31), yet the precise mechanisms by which these condensates modulate gene transcription at native chromatin remain elusive. A unique feature of LAMPS is the ability to capture de novo–formed condensates in situ for biochemical and mechanistic studies (Fig. 1A). This is achieved by streptavidin-based affinity purification of biotinylated dCas9-tethered protein-DNA complexes at endogenous genomic loci (21, 22).

To validate the LAMPS approach for identifying the macromolecular composition of locus-specific nuclear condensates in living cells, we first sought evidence for on-target association of LAMPS complexes at the sgRNA-targeted *HS2* enhancer. Upon stable expression of dCas9-CRY2^{Clust}-FUS^N or dCas9-CRY2^{Clust}-BRD4ΔN with or without sg*HS2* in HeLa cells, the dCas9-tethered chromatin was cross-linked, fragmented, and affinity-purified using streptavidin magnetic beads, followed by analysis of the captured DNA using the LAMPS–chromatin immunoprecipitation (ChIP) assay (Fig. 4A) (21, 22, 24). We observed significant dCas9 enrichment at the *HS2* locus (852- to 1687-fold relative to nontargeting sgRNA control; Fig. 4B), indicating efficient recruitment of LAMPS complexes to native chromatin. Moreover, on-target dCas9 signal further increased upon light induction likely because of LAMPS-mediated clustering. To evaluate specificity, we performed deep sequencing of dCas9-bound genomic DNA. Notably, the recruitment of dCas9 by sg*HS2* resulted in enrichment of *HS2* with few nonspecific dCas9 binding regions, including predicted off-targets, at genome scale (Fig. 4C and fig. S4, A and B). These chromatin assays provide evidence that LAMPS complexes are highly enriched at the dCas9/sgRNA-targeted genomic loci.

Altered chromatin accessibility and DNA looping by LAMPS-activated condensation

We next sought to address how LAMPS-induced condensation mechanistically activates gene transcription. We hypothesized that de novo condensation creates a local chromatin environment permissive for recruitment of TFs and coactivators through IDR-mediated multivalent interactions. To test this, we performed assay for transposase-accessible chromatin using sequencing (ATAC-seq) to assess chromatin accessibility at LAMPS-targeted *HS2* before and after blue light illumination. Despite strong enrichment of sgRNA-mediated dCas9 binding at *HS2* (Fig. 4, B and C), no detectable ATAC-seq signal was observed before illumination (fig. S5A),

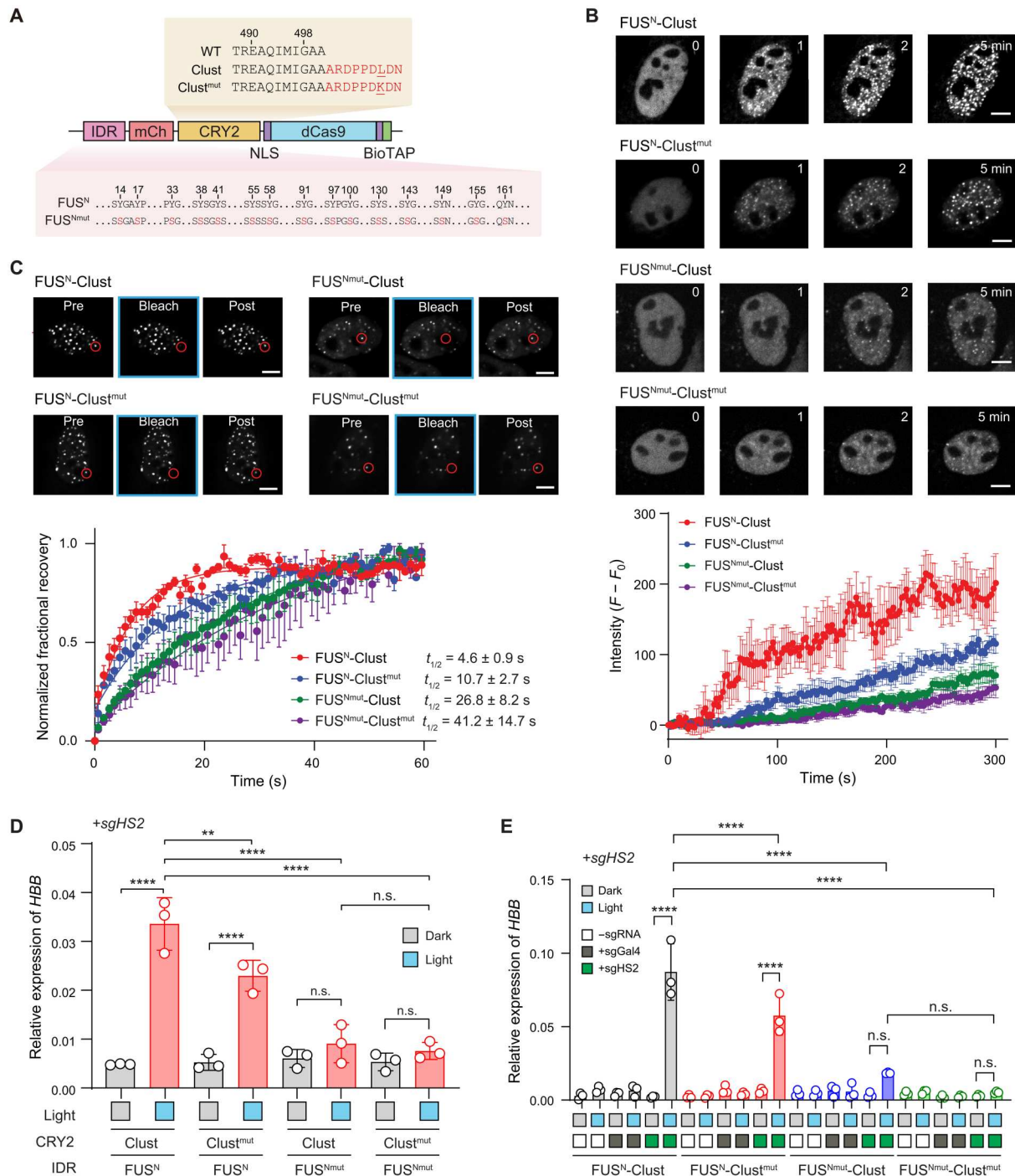


Fig. 3. Molecular determinants of LAMPS-mediated condensation. (A) Schematic of LAMPS with mutant CRY2^{Clust} and/or FUS^N modules. The L7K substitution mutations in the C terminus of CRY2^{Clust} are underscored. The Tyr-to-Ser substitutions in FUS^N mutant (FUS^{Nmut}) are highlighted in red. (B) Time-lapse confocal images and fluorescence intensities of light-induced condensates harboring single or combined mutations in CRY2^{Clust} or FUS^N versus the WT control in HeLa stable cells. The quantification of normalized fluorescence intensity and the half-life ($t_{1/2}$) of maximal intensity are shown. Results are means \pm SEM ($N = 5, 5, 5,$ and 7 cells for the indicated FUS^N-fused dCas9-CRY2 variants, respectively). (C) Confocal images are shown for FRAP assays of LAMPS condensates harboring single or combined mutations in CRY2^{Clust} or FUS^N versus the WT control in HeLa stable cells. The red circles indicate the region bleached by 0.1% laser power for 1 ms, followed by time-lapse imaging of fluorescence redistribution. The quantification of normalized fractional recovery and the half-life ($t_{1/2}$) are shown. Results are means \pm SEM ($N = 3$ independent experiments). (D) Analysis of *HBB* mRNA expression in HeLa cells transiently coexpressing LAMPS harboring single or combined mutations in CRY2^{Clust} or FUS^N relative to the WT control and sgHS2, with or without blue light illumination. The mRNA expression relative to *GAPDH* is shown. Results are means \pm SD ($N = 3$ independent experiments) and analyzed by one-way ANOVA. P values were calculated by comparing samples under dark and light conditions. $**P < 0.01$ and $****P < 0.0001$. (E) Analysis of *HBB* mRNA expression in HeLa cells stably coexpressing LAMPS harboring WT or mutant CRY2^{Clust} or FUS^N along with nontargeting sgGal4 or sgHS2. Results are means \pm SD ($N = 3$ independent experiments) and analyzed by one-way ANOVA. $****P < 0.0001$.

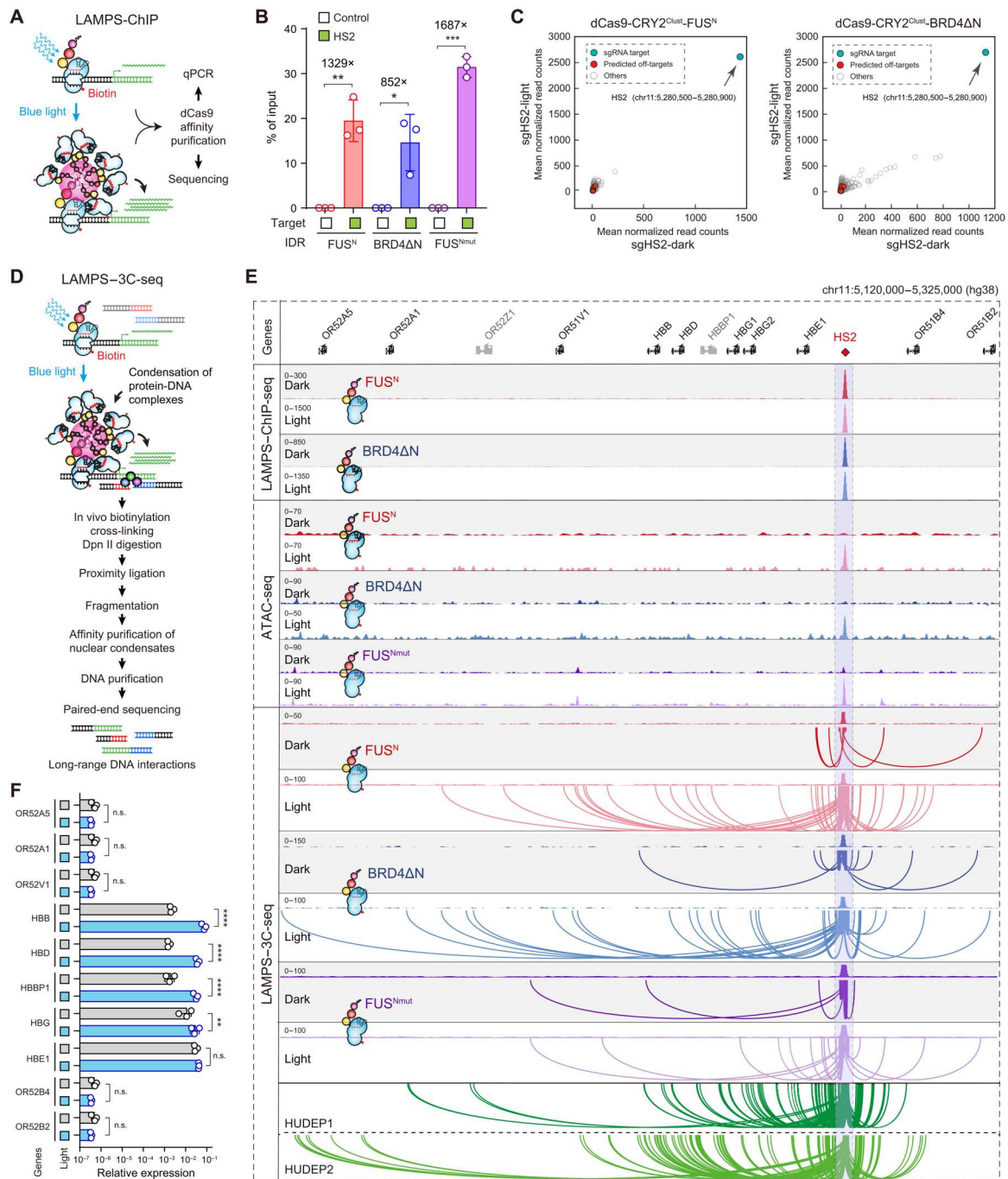


Fig. 4. LAMPS-mediated condensation reconfigures chromatin structure. (A) Schematic of LAMPS-ChIP to assess specificity of LAMPS-mediated targeting to endogenous genomic loci. (B) The enrichment of dCas9 binding to the sgRNA-targeted *HS2* enhancer in stable cells coexpressing dCas9-CRY2^{Clust}-FUS^N, dCas9-CRY2^{Clust}-BRD4ΔN, or dCas9-CRY2^{Clust}-FUS^{Nmut} with or without sgHS2. The percentage of input by LAMPS-ChIP analysis is shown. Fold enrichment relative to nontargeting control primers is labeled. Results are means ± SD (*N* = 3 independent experiments) and analyzed by two-sided *t* test. **P* < 0.05 and ***P* < 0.01. (C) Genome-wide analysis of dCas9 binding in HeLa stable cells coexpressing dCas9-CRY2^{Clust}-FUS^N or dCas9-CRY2^{Clust}-BRD4ΔN with sgHS2 under the dark or light condition. Data points for the sgRNA target regions are shown by arrows and green circles, and the predicted off-targets and nonspecific binding sites are shown as red and gray circles, respectively. The y axis and x axis denote mean normalized read count under the dark and light conditions from two independent CHIP-seq experiments, respectively. (D) Schematic of LAMPS-3C-seq involving biotinylated dCas9-mediated affinity capture of targeted genomic loci followed by 3C analysis. (E) Genome browser view of dCas9 binding (by LAMPS-ChIP-seq), chromatin accessibility (by ATAC-seq), and locus-specific chromatin interactions (by LAMPS-3C-seq) in HeLa stable cells coexpressing dCas9-CRY2^{Clust}-FUS^N or dCas9-CRY2^{Clust}-BRD4ΔN with sgHS2 under the dark or light conditions. Contact profiles including the density map and long-range DNA interactions (or loops) compiled from two independent experiments are shown. *HS2*-mediated chromatin interactions in HUDEP1 and HUDEP2 erythroid cells are also shown. (F) Analysis of mRNA expression of genes proximal to LAMPS-targeted *HS2* enhancer in HeLa cells stably coexpressing dCas9-CRY2^{Clust}-FUS^N with or without blue light illumination. Fold increases relative to dark is labeled. Results are means ± SD (*N* = 3 independent experiments) and analyzed by one-way ANOVA. ***P* < 0.01 and *****P* < 0.0001.

suggesting that dCas9 binding alone has little effect on accessibility. By contrast, light-activated condensation increased chromatin accessibility at *HS2* for both dCas9-CRY2^{Clust}-FUS^N and dCas9-CRY2^{Clust}-BRD4ΔN (Fig. 4, D and E, and fig. S5A). Notably, cells expressing the mutant FUS^{Nmut} also displayed increased chromatin accessibility upon blue light illumination (Fig. 4E), suggesting that LAMPS clustering is sufficient to modulate chromatin accessibility at the target loci but the IDR-mediated composition of condensates is required for subsequent gene activation. These results support the model by which LAMPS-induced nuclear condensation increases chromatin accessibility to facilitate the recruitment of TFs, enabling the assembly of transcriptional complexes for gene activation.

Chromatin organization maintained by long-range DNA interactions such as enhancer-promoter looping is critical for transcriptional regulation (32). Given the unique feature of LAMPS for unbiased analysis of locus-regulating chromatin interactions (21, 22), we examined *HS2*-associated chromatin looping before and after light-activated condensation. Upon coexpression of dCas9-CRY2^{Clust}-FUS^N or dCas9-CRY2^{Clust}-BRD4ΔN with sg*HS2*, long-range DNA contacts associated with dCas9-targeted *HS2* were cross-linked, followed by Dpn II digestion and proximity ligation of interacting DNA fragments. Locus-specific interactions were captured by streptavidin-based purification of biotinylated dCas9 and analyzed by paired-end sequencing using the LAMPS-3C sequencing (3C-seq) assay (Fig. 4D).

Using this approach, we first noted sparse and spurious interactions at *HS2* before illumination, consistent with low basal enhancer activity in HeLa cells (Fig. 4E and fig. S5B). By contrast, we detected increased numbers and distances of long-range DNA interactions for both dCas9-CRY2^{Clust}-FUS^N and dCas9-CRY2^{Clust}-BRD4ΔN after blue light illumination. The identification of DNA loops between the *HS2* enhancer, *HBB* and *HBD* promoters, and *HBBP1* intergenic regions is consistent with their roles in β -globin transcription (21, 33, 34). We observed significant up-regulation of the *HBB*, *HBD*, and *HBBP1* genes, which were associated with more consistent enhancer-promoter loop formation, but variable or no change in the expression of the more distal and silent olfactory genes (Fig. 4F). We performed parallel experiments with FUS^{Nmut} LAMPS and observed reduced long-range chromatin interactions, including known enhancer-promoter loops (Fig. 4E and fig. S5B), consistent with a critical role for IDRs in LAMPS-mediated condensation and gene activation (Fig. 3). Together, these results demonstrate that LAMPS-mediated condensation induces de novo formation of chromatin loops, providing direct evidence for the emergent model that the condensation of macromolecules may represent the biophysical force to structure the three-dimensional (3D) genome (17).

Notably, LAMPS-activated HeLa cells contained fewer long-range interactions compared to *HS2*-associated interactions in embryonic/fetal-stage human umbilical cord blood-derived erythroid progenitor cells (HUDEP1) or adult-stage (HUDEP2) erythroblasts that endogenously express β -globin genes (Fig. 4E) (35, 36). Hence, while LAMPS-mediated condensation is sufficient to initiate chromatin looping for gene activation, the stabilization and/or propagation of these loops likely require additional mechanisms such as the action of lineage-specific TFs, the recruitment of specific chromatin regulators, and/or the epigenetic state of local chromatin.

Reconfiguration of proteomic composition for gene activation by LAMPS-activated condensation

Biomolecular condensation is recognized as a fundamental mechanism underlying diverse intracellular structures, yet little is known of their regulatory composition under physiological conditions where their functional consequences have been established. Having demonstrated the biophysical properties of LAMPS-activated nuclear condensates and the determinants for their effects on gene transcription and chromatin configuration, we next sought to elucidate the molecular composition and dynamics of light-induced condensates in living cells.

To this end, we leveraged the biotinylated dCas9 moiety and performed proteomic analysis of purified LAMPS-induced condensates (Fig. 1A). Specifically, HeLa cells stably expressing dCas9-CRY2^{Clust}-FUS^N (or with FUS^{Nmut}) and sg*HS2* were illuminated with blue light and immediately cross-linked to stabilize condensate-chromatin interactions, while nonilluminated cells were processed in parallel as a negative control. Stringent urea washes were performed to remove cytoplasmic and nuclear soluble fractions and to enrich chromatin-bound complexes; this step is also intended to deplete nonchromatin bound condensates nucleated by CRY2 clustering to further enrich for on-target condensates (21). Condensate-associated proteins cross-linked to chromatin were then isolated and copurified with dCas9 using streptavidin-conjugated magnetic beads, followed by on-bead trypsin digestion and mass spectrometry-based proteomic profiling (Fig. 5A).

We identified 258 and 184 significantly enriched or depleted nuclear proteins, respectively, in light-activated condensates relative to nonilluminated controls (\log_2 fold change ≥ 1 or ≤ -1 , $P < 0.01$ from three replicate experiments; table S1). Notably, RNA polymerase II (Pol II) subunits (POLR2B, POLR2G, and POLR2I), general TFs (TAF1, TAF2, and GTF2F1), transcriptional coactivators (EP300, PAF1, and CCNT1), mediators (MED1, MED23, and MED24), and cohesin complexes (RAD21, SMC1A, SMC1B, and SMC3) were among the top enriched proteins. By contrast, epigenetic corepressors including human silencing hub (HUSH) subunits PPHLN1, FAM208A, and MPHOSPH8 (37, 38), RNA splicing factors, and nuclear lamins (LMNA and LMNB1) were the top depleted proteins in LAMPS-induced condensates (Fig. 5B). To identify candidate cellular pathways relevant to LAMPS-induced condensation, we performed gene ontology and pathway analyses of the enriched or depleted proteins. Chromatin organization, regulation of gene transcription, and nucleic acid binding were among the top enriched biological processes or molecular functions, whereas RNA splicing, DNA packaging, and nuclear organization were associated with the depleted proteins (Fig. 5C and table S2). The enrichment and depletion of distinct protein complexes supports the notion that nuclear condensation provides a mechanism to selectively partition proteins into compartmentalized, higher-order assemblies to regulate gene transcription (39). To validate candidate condensate-associated proteins identified from proteomics, we examined the chromatin occupancy of RNA Pol II (RPB1) and cohesin subunits (RAD21 and SMC1). We detected enrichment of Pol II and cohesin after light illumination at *HS2* but not at nontargeted genomic loci (fig. S6A), consistent with their recruitment to LAMPS-targeted condensates.

By parallel analysis of the proteomic composition of LAMPS-activated condensates with the mutant (FUS^{Nmut}) IDR, we observed a nearly complete loss of enriched coactivators and chromatin

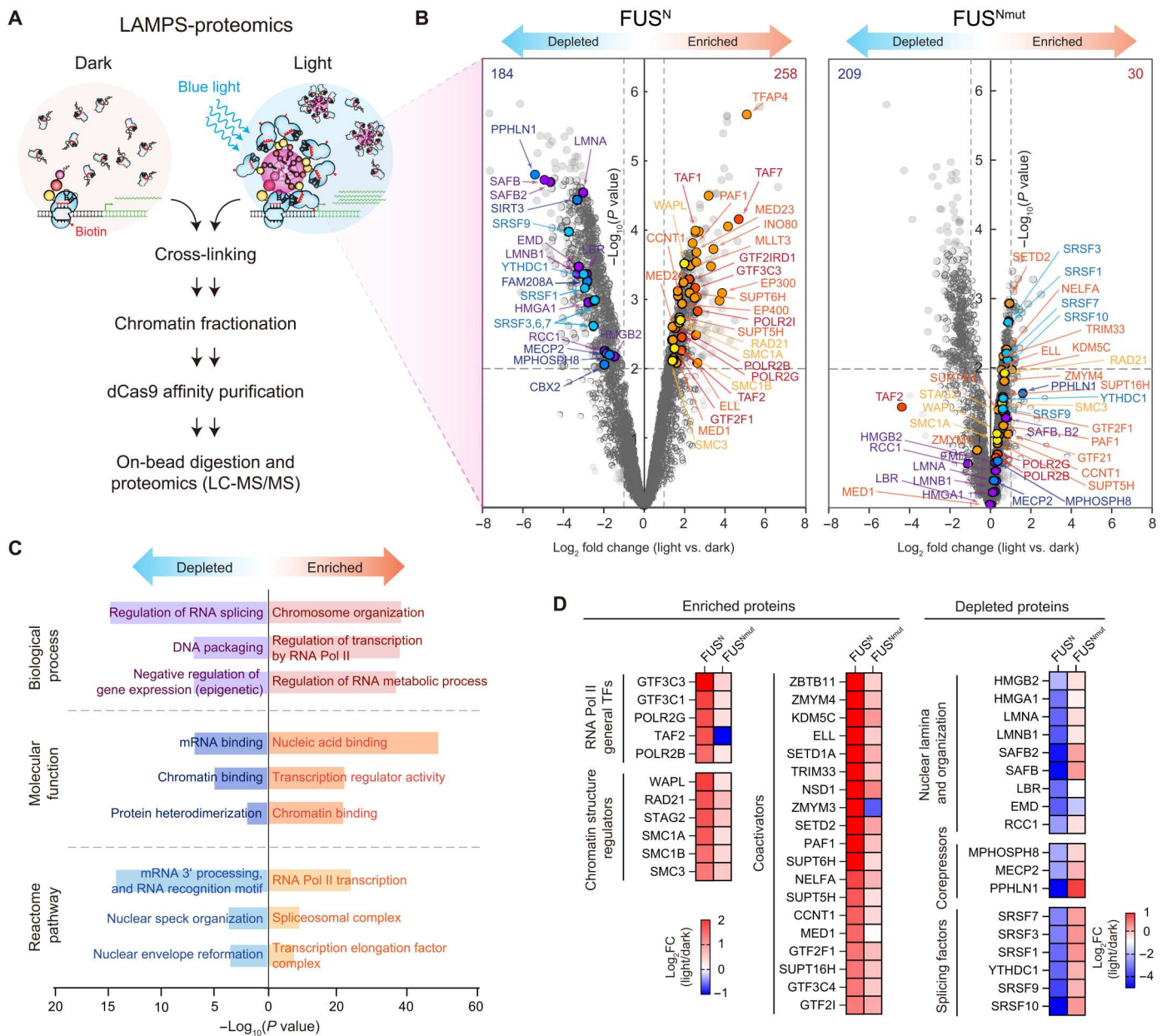


Fig. 5. LAMPS-activated condensation reorganizes proteomic composition. (A) Schematic of LAMPS-proteomics by comparative proteomic profiling of LAMPS-activated nuclear condensates. (B) LAMPS-proteomic profiling of protein composition of light-induced nuclear condensates in HeLa cells stably coexpressing dCas9-CRY2^{Clust}-FUS^N or dCas9-CRY2^{Clust}-FUS^{Nmut}. Relative protein levels in biotinylated dCas9-captured protein complexes under light versus dark conditions are plotted on the x axis as mean \log_2 fold changes across three replicate experiments. Negative \log_{10} transformed P values are plotted on the y axis. Significantly enriched proteins (\log_2 fold change ≥ 1 or ≤ -1 , $P < 0.01$) are denoted by colored or black dots, all others by gray dots. Dotted lines indicate \log_2 fold change = 1 or -1 (x axis) and P value of 0.01 (y axis). Representative proteins enriched or depleted in LAMPS-induced condensates relative to dark control samples are denoted by colored arrowheads and listed. (C) Pathway analysis of LAMPS-enriched or LAMPS-depleted proteins. The top enriched or depleted pathways in biological process, molecular function, and Reactome pathway are shown. (D) Heatmap of the \log_2 fold enrichment (light/dark) for representative groups of TFs enriched or depleted in condensates harboring WT versus mutant FUS^N IDR.

structure factors identified from native IDR-mediated condensates (Fig. 5, B and D, and fig. S6B). IDR mutation also abrogated the selective depletion of nuclear lamina proteins and corepressors associated with the native IDR. These results, together with the analyses of condensate properties (Fig. 3, A to C), gene transcription (Fig. 3, D and E), and long-range chromatin looping (Fig. 4E),

provide strong support for a dominant role of IDRs in mediating the selective compartmentalization of nuclear factors into LAMPS-seeded condensates for gene activation.

Together, by profiling the proteome composition and 3D conformation of light-activated nuclear condensates in living cells, we provide evidence that inducible condensate formation at an

endogenous enhancer element facilitates the selective recruitment of TFs, chromatin regulators, and RNA binding proteins, with concomitant depletion of repressor complexes, to induce chromatin remodeling and gene activation (Fig. 6). Therefore, by engineering LAMPS-activated condensation in living cells, our findings support a model whereby targeted formation of macromolecular condensates induces reconfiguration of chromatin architecture and accessibility to modulate gene transcription.

DISCUSSION

Conventional models of gene activation posit that cooperative binding of TFs to gene-proximal promoters and/or gene-distal enhancers mediates long-range DNA looping through protein-protein interactions, triggering the recruitment of additional coactivators to assemble the transcriptional complexes (40). A revised conceptual model was recently proposed invoking condensation of LCD-containing TFs as the biophysical basis by which long-range DNA contacts are nucleated between distal CREs and gene-proximal promoters, establishing so-called “transcriptional hubs” (9, 12, 41), although direct evidence is still lacking. Several recent studies demonstrated that condensation of TFs can activate transcription by measuring reporter gene expression or global nascent transcripts. Specifically, engineered TetR-containing TF droplets mediated by FUS^N was shown to aggregate at the promoter of a reporter gene to activate its expression in mammalian cell lines (18). In addition, TAF15, another FET family TF, is recruited by RNA Pol II to amplify global gene expression through heterotypic condensation with the C terminus of RNA Pol II (42). However, other studies have also argued that gene activation by TFs occurs independently of condensation. For example, using inducible TF droplet systems targetable to knock-in LacO reporter loci, it was found that reporter gene activation occurs primarily via multivalent protein recruitment and TF supersaturation is inhibitory for gene activation (43). Another study showed that the overexpressed LCD of Ewing sarcoma (EWS) TF is incorporated into endogenous EWS-FLI1 puncta in EWS cells but condensate formation repressed EWS target gene transcription (44). Although these approaches provide crucial insights into the relationship between TF condensation and gene transcription, they do not allow for simultaneous analyses of changes in gene activity, chromatin structure, and interactions caused by induced condensation at endogenous loci. The macromolecular composition of nuclear condensates and the mechanisms

underlying their formation and function in native chromatin remain largely unexplored.

In this study, we introduce a bipartite method for light-activated formation of nuclear condensates at native chromatin and biochemical interrogation of their molecular consequences. This system leverages two unique features, CRY2-based optogenetics (45) and biotinylated dCas9-mediated chromatin capture (21), to dissect the roles of condensate formation in gene regulation. Using the human β -globin *HS2* enhancer as a testbed genomic locus, we establish evidence that light-activated nuclear condensates can induce selective TF recruitment and chromatin accessibility at targeted genomic loci. LAMPS-mediated condensation induces de novo formation of long-range chromatin interactions including enhancer-promoter loops to activate endogenous gene transcription. These results are consistent with recent findings that oncogenic translocations involving fusion of IDR domains to chromatin-binding TFs drive condensation and aberrant chromatin loop formation in cancer cells (46).

Biomolecular condensation is recognized as a fundamental mechanism for the compartmentalization of intracellular biochemical processes (3, 20). In the nucleus, the formation of nanoscale transcriptional condensates has been described to control several steps of gene activation including the formation of preinitiation complexes, transcriptional pausing and elongation, super-enhancer clustering, and mRNA splicing and processing (9–12, 30, 41). Despite these findings, little is known about whether and how distinct molecular compositions of condensates contribute to biological processes under physiological contexts. Here, we attempted to address this question using dCas9-mediated genome targeting and biotin-streptavidin-based affinity capture to characterize the regulatory composition of light-induced condensates in living cells. We identified an ensemble of nuclear proteins specifically enriched in LAMPS-induced condensates, including factors associated with basal transcriptional machinery, general TFs, coactivators, and chromatin structure proteins. The identification of chromatin looping factors (e.g., every subunit of the cohesin complex) and transcriptional apparatus (e.g., RNA Pol II subunits) is consistent with our findings of increased chromatin accessibility and de novo formation of long-range chromatin loops. Moreover, we identified nuclear factors depleted in LAMPS-induced condensates. These include epigenetic repressors associated with heterochromatin formation, such as known subunits of the HUSH complex associated with retrotransposon silencing (37, 38) and nuclear lamina

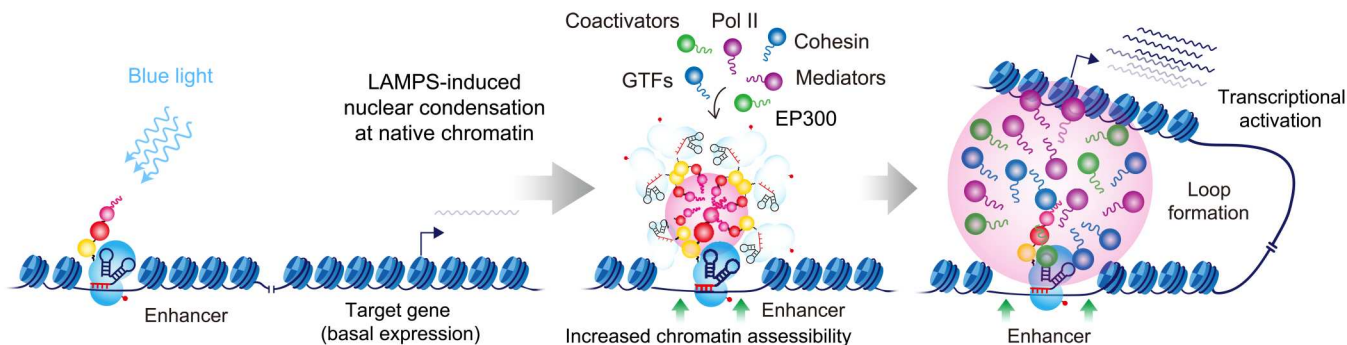


Fig. 6. Nuclear condensation modulates gene transcription by chromatin reconfiguration. Schematic of the model for LAMPS-mediated nuclear condensation in transcriptional regulation.

and organization proteins. Crucially, the differential enrichment and depletion of distinct factors in LAMPS-induced condensates is dependent on IDR-mediated multivalent interactions, as IDR mutation abrogates these profiles, consistent with the notion that condensate formation provides a mechanism to selectively compartmentalize protein complexes into higher-order assemblies for gene regulation.

In considering LAMPS for studying the structure and function of nuclear condensation, the following caveats are warranted. First, while our chromatin assays provide strong support for LAMPS on-target association and biological impact, one limitation of this work is the absence of direct microscopic evidence for condensate colocalization with the target loci. Experiments such as immunofluorescence coupled with DNA fluorescence in situ hybridization may resolve this outstanding issue, although such an approach has proved technically challenging. Second, although our findings validate the requirement of IDR-dependent condensation in LAMPS-mediated remodeling of condensate composition for gene activation, it remains possible that IDR mutation also impairs key residues supporting protein-protein interaction with transcriptional cofactors (47, 48). It will be important in future studies to deconvolute which residues in IDRs support condensate formation versus direct protein interaction. We envision that the modularity of the LAMPS system can facilitate the systematic residue-by-residue interrogation of the relative contribution of condensation versus protein-protein interaction by TF activation domains on endogenous gene transcription. Third, while LAMPS-proteomics enables the unbiased identification of candidate regulators specifically enriched or depleted in LAMPS-induced condensates, some of the identified factors might not directly associate with the targeted genomic loci because of condensation of indirect interactions and/or nonchromatin-associated dCas9 that are residually enriched. Hence, the roles of candidate “client” proteins in LAMPS-mediated gene activation warrant further investigation. By contrast, the LAMPS-ChIP and LAMPS-3C-seq assays, which are based on analyzed dCas9-bound DNA elements, are capable of quantifying LAMPS-induced effects at the dCas9-targeted genomic loci. Last, while we showcased the applications of LAMPS by focusing on two exemplary IDRs, the macromolecular composition and functional effects on gene transcription by other IDRs also require further investigation. Comparing similarities and/or differences in nuclear condensates formed through various IDR modules in living cells will be necessary to nominate a comprehensive set of candidate factors that regulate condensation-mediated gene transcription.

By developing a new approach that enables parallel analyses of changes in gene transcription, chromatin configuration, and macromolecular composition caused by light-activated nuclear condensation, we conclude that inducible condensation at gene-distal enhancers can increase chromatin accessibility to facilitate the recruitment of TFs, coactivators, and chromatin architecture proteins, resulting in the formation of long-range chromatin interactions between enhancers and gene-proximal promoters to activate gene transcription (Fig. 6). Consistent with this model, recent studies using quantitative imaging of transcriptional bursting suggest that enhancer activation correlates with the temporal frequency of enhancer-promoter interactions and TF occupancy (49). Therefore, the cooperative nucleation of proteins and nucleic acids into biomolecular condensates at both enhancers and promoters and their subsequent interactions across nuclear space could provide the driving

force to spatially approximate otherwise distant CREs together. Note that RNA molecules are also recognized as essential components in condensation and may modulate the viscosity and dynamics of phase-separated condensates (8, 31, 50, 51). RNA itself can physically interact with RNA binding molecules and splicing factors through multivalent interactions to facilitate condensate formation. In this study, we note the depletion of RNA splicing factors in LAMPS-induced condensates, consistent with the notion that condensation may enable selective compartmentalization of protein complexes by IDR-mediated multivalent interactions. Further studies are needed to determine the contribution of different RNA species and RNA-interacting proteins to LAMPS-mediated condensate formation and gene activation. The biotinylated dCas9 affinity capture in the LAMPS design allows for copurification of chromatin-associated RNAs that may be incorporated into nuclear condensates for gene regulation (21).

Given its modular design and programmability, we envision LAMPS to be broadly applicable for dissecting the structure-function relationship of biomolecular condensation across biological contexts, such as by designing sgRNAs for specific loci of interest and/or by fusing alternative IDR domains, including mutants such as the FUS^{Nmut} demonstrated here. The latter may present a versatile paradigm to assess the pathological roles of nuclear phase transition as undercharacterized mechanisms of human disease (46).

MATERIALS AND METHODS

Cell culture

HeLa cells were obtained from the American Type Culture Collection (ATCC, catalog no. CCL-2) and validated by short tandem repeat profiling analysis by the vendor and were free of mycoplasma contamination. Cells were cultured in Dulbecco's modified Eagle's medium (DMEM) containing 10% fetal bovine serum (FBS) and 1% penicillin/streptomycin. For lentivirus production, human embryonic kidney (HEK) 293T cells were cultured in DMEM with 1× GlutaMAX and 1× sodium pyruvate at 37°C with 5% CO₂.

Cloning of LAMPS vectors

CRY2 variants

CRY2 mutations (E490G or E490R) were individually introduced to the mCh-CRY2-PHR (residues 1 to 498)-STIMct vector (52) using the QuikChange Lightning Multi Site-Directed Mutagenesis Kit (Agilent Technologies). The C-terminal extension of CRY2-PHR (CRY2^{Clust}) was generated by a polymerase incomplete primer extension cloning strategy to add the additional 9-mer peptide “ARDPPDLDN.” The CRY2^{Clust} L7K mutant was generated by polymerase chain reaction (PCR) mutagenesis with primers encoding the desired point mutation followed by In-Fusion cloning. The dCas9 fragment from the pLVX-EF1α-dCas9-CBio-IRES-zsGreen1 vector (CAPTURE2.0-Cbio; Addgene, #138418) (22) flanked with Xma I and Bgl II sites was subcloned into the CRY2 variant-containing vectors to replace STIMct between Bsp EI and Bam HI sites. PCR amplifications were performed using a KOD Start DNA polymerase (EMD Millipore).

IDR domain fusion

The N terminus of FUS (FUS^N) and the N terminus-less BRD4 (BRD4ΔN) (6, 17, 53) were cloned to generate IDR-fused dCas9-CRY2 variants (fig. S1A). Specifically, for FUS^N fusion, the cDNA

sequence encoding FUS^N was PCR-amplified using New England Biolabs (NEB) Phusion high-fidelity PCR kit and cloned upstream of CRY2 variant-containing constructs by Nhe I digestion. The dCas9 fragment was fused to the C terminus of CRY2-PHR as described above. BRD4 Δ N was cloned from the full-length BRD4 cDNA [a gift from C.-M. Chang at University of Texas Southwestern Medical Center (UTSW)]. The 15 Tyr-to-Ser FUS^N IDR mutant template was generated by PCR amplification with NEB Q5 HiFi polymerase from a synthesized gene block ordered from Genewiz. FUS^N or BRD4 Δ N sequences containing 15–base pair (bp) homology arms were cloned into the Nhe I-linearized LAMPS vectors (100 ng) using an In-Fusion HD cloning kit (Clontech). All primer sequences are listed in table S3.

sgRNA cloning

sgRNAs for site-specific targeting of genomic regions were designed to minimize off-target cleavage based on publicly available filtering tools (<http://crispor.tefor.net/>). To minimize potential interference between the chromatin binding of dCas9 and trans-acting factors, sgRNAs were designed to target the proximity of CREs as previously described (21, 22). Two sgRNAs were used per target site. The oligonucleotides for sgHS2 or sgBCL11A (table S3) were phosphorylated and annealed in the following reaction: 10 μ M guide sequence oligo, 10 μ M reverse complement oligo, T4 ligation buffer (1 \times), and 5 U of T4 polynucleotide kinase (NEB) with the cycling parameters of 37°C for 30 min followed by 95°C for 5 min and then ramp down to 25°C at 5°C/min. The annealed oligos were cloned into the sgRNA vectors using a Golden Gate Assembly strategy including the following: 100 ng of circular sgRNA vector plasmid, 0.2 μ M annealed oligos, NEBuffer 2.1 (1 \times), 20 U of Bbs I restriction enzyme (NEB), 0.2 mM adenosine triphosphate, bovine serum albumin (0.1 mg/ml), and 750 U of T4 DNA ligase (NEB) with the cycling parameters of 20 cycles at 37°C for 5 min and 20°C for 5 min, followed by 80°C for 20 min.

Transient transfection

HeLa cells were seeded into six-well or 35-mm plates at 50% confluent cell density overnight and then transfected with LAMPS vectors with or without sgRNAs (two independent sgRNAs per target mixed at 1:1 ratio) using Lipofectamine 3000 following the manufacturer's protocol (Invitrogen, L3000075). Briefly, solution A was prepared with 125 μ l of Opti-MEM I reduced serum medium (Gibco) and 3.75 μ l of Lipofectamine 3000. Solution B was prepared with 125 μ l of Opti-MEM, 1.5 μ g of LAMPS and 1 μ g of sgRNA vector DNA (2.5 μ g of DNA total), and 5 μ l of P3000 enhancer. Solutions A and B were vortexed briefly, pooled, and incubated for 5 to 10 min at room temperature. The mixture was added to the cells dropwise. Cells were harvested for imaging or gene expression analyses 24 to 48 hours posttransfection.

Lentiviral transduction and generation of stable cell lines

Lentiviruses containing sgRNAs (mixed at 1:1 ratio for two independent sgRNAs) or LAMPS constructs were packaged in HEK293T cells using Lipofectamine 3000 with the following modifications: 6.5 μ g of psPAX2 (Addgene, #12260), 3.5 μ g of VSV-G (Addgene, #8454), and 10 μ g of pLenti expression vector (dCas9 or sgRNAs) were cotransfected using Lipofectamine 3000 into HEK293T cells on a 10-cm petri dish with DMEM at 37°C with 5% CO₂. After incubation for 6 hours, transfected DMEM was

changed with 6 ml of prewarmed lentivirus packaging media (Opti-MEM I reduced serum medium with GlutaMAX, supplemental with final concentrations of 5% FBS and 0.2 mM sodium pyruvate). Lentiviral particles were then harvested from the supernatant at 48 and 72 hours posttransfection, pooled, and centrifuged briefly to clear cell debris. The viral supernatant was precipitated using the PEG-it Virus Precipitation Solution (Systems Biosciences) following the manufacturer's instructions. To transduced cells, concentrated viral suspensions were added dropwise to target cells at \geq 95% confluent cell density in growth media containing polybrene (10 μ g/ml), incubated for 24 hours before changing to fresh media, and then recovered for 2 to 3 days at 37°C followed by fluorescence-activated cell sorting (FACS) for high dCas9/mCherry-expressing cells. Sorted cells were expanded to be transduced with sgRNA-expressing lentiviruses. To obtain cells with a high sgRNA expression, the top 5% of zsGreen-positive cells were FACS-sorted 48 hours posttransfection and selected with puromycin (1 μ g/ μ l). The sequences for sgRNAs are listed in table S3.

Gene expression analysis

LAMPS-activated formation of nuclear condensates

To induce LAMPS-mediated condensates, HeLa stable cells or transiently transfected cells were cultured overnight in 35-mm glass-bottom plates with DMEM. To minimize effects due to variation in transient transfection efficiency of each LAMPS construct, cells with comparable mCherry signal were FACS-sorted 24 hours after transfection. Cells were incubated in 1 \times phosphate-buffered saline (PBS) buffer during imaging experiments to remove phenol red. Cells were illuminated with blue light (488 nm) using a Nikon SMZ18 stereomicroscope system for 5 min at room temperature immediately after addition of 1 \times PBS. We used a Nikon INTENSILIGHT-CHGFI lamp module (P2-EFL filter cube GFP-B). The blue light intensity was 0.35 mW/cm² and measured by the Thorlabs optical power meter PM100D. Blue light-exposed cells were incubated in DMEM at 37°C for 30 min before harvesting for gene expression analysis. Control cells without light exposure (dark) were prepared in parallel but incubated in the dark room and shielded from light using aluminum foil-wrapped 15-cm petri dish for 5 min.

Reverse transcription quantitative PCR

RNA was isolated using the TRIzol extraction method as previously described (54). cDNA was generated using an iScript DNA synthesis kit (Bio-Rad). Reverse transcription quantitative PCR (RT-qPCR) was performed using the iQ SYBR Green Supermix (Bio-Rad) and cycled using a CFX 384 Touch Real Time PCR Detection system (Bio-Rad). Primer sequences are listed in table S3.

Fluorescence imaging

HeLa cells were plated on glass-bottom dishes (Cellvis, catalog no. D35-20-0-TOP) and transfected with LAMPS constructs using Lipofectamine 3000. Fluorescence imaging was performed 24 hours posttransfection on a Nikon Ti2 inverted epifluorescence microscope with a Yokogawa W1 dual spinning disk scan head equipped with six solid-state lasers (405, 445, 488, 514, and 640 nm) for imaging and one additional laser for stimulation (473 nm). Fluorescence images were captured using a Photometrics Prime BSI and back-side illuminated scientific complementary metal-oxide-semiconductor (sCMOS) camera. For time-lapse imaging, a 60 \times oil lens was used for high-resolution images and conducted with an Okolab

Stage Top incubator, which provides incubation with full environmental control including heating, humidity, and CO₂ regulation. Blue light illumination was performed with the built-in 488-nm laser source (5% input). The fluorescence intensities of light-induced puncta were calculated by the NIS-Elements AR microscope imaging software (Nikon, NIS-element AR version 4.0). To quantify the area of puncta, puncta were selected as the region of interest (ROI); the area of ROIs was then analyzed by the NIS-Elements software. The changes in puncta intensity ($F - F_0$) were calculated by measuring the local intensity changes of puncta, where F is the fluorescence at time t and F_0 is the fluorescence before blue light illumination.

Fluorescence recovery after photobleaching

FRAP was carried out by bleaching a defined area with 0.1% laser power for 1 ms after 5 min of illumination. The images were taken before and immediately after bleaching, followed by consecutive imaging every 1 s. Fluorescence intensity was measured using the NIS-Elements AR microscope imaging software. To analyze fluorescence recovery in Fig. 2D, fluorescence intensity was normalized to the intensity before bleaching (i.e., $F = F_t/F_0$, where F_t is the fluorescence at time t and F_0 is the fluorescence before bleaching). To analyze fluorescence recovery in Figs. 2E and 3C, the normalized fractional recovery was calculated by $(F_t - F_{\text{bleach}})/(F_{\text{max}} - F_{\text{bleach}})$, where F_t is the fluorescence at time t , F_{max} is the maximal fluorescence after photobleaching, and F_{bleach} is the fluorescence at bleaching.

LAMPS-ChIP sequencing

Streptavidin affinity purification of dCas9-captured DNA and sequencing

A total of 1×10^7 LAMPS-expressing HeLa stable cells transduced with sequence-specific sgRNAs or no sgRNA (control) were harvested, cross-linked with 1% formaldehyde (Sigma-Aldrich) for 10 min with gentle rocking, and quenched with final concentration of 0.125 M glycine for 5 min at room temperature. Cross-linked cells were washed twice with $1 \times$ PBS and then lysed in 1 ml cell lysis buffer [25 mM tris-HCl (pH 7.4), 85 mM KCl, and 0.1% Triton X-100] freshly supplemented with 1 mM dithiothreitol (DTT) and 1:100 protease inhibitor cocktail (APEX-BIO) and rotated for 30 min at 4°C. Cell lysates were centrifuged at 2300g for 5 min at 4°C to isolate the nuclei. Nuclei were suspended in 500 μ l of 0.5% SDS lysis buffer [0.5% SDS, 10 mM EDTA, and 50 mM tris-HCl (pH 8.0)] and sonicated to shear chromatin fragments to an average size between 200 and 500 bp using a Branson Sonifier 450 ultrasonic processor (20% amplitude, 0.5-s on/1.0-s off for 30 s in total or 60 pulses). Sheared chromatin was centrifuged at 16,100g for 10 min at 4°C. A total of 450 μ l of the supernatant was transferred to a new 1.5-ml Lo-Bind Eppendorf tube and supplemented with a final concentration of 300 mM NaCl and then incubated with 20 μ l of Streptavidin Dynabeads MyOne T1 (Thermo Fisher Scientific, #65602 or Invitrogen, #656-01) at 4°C overnight with rotation. Beads were prewashed twice with ChIP dilution buffer [0.1% SDS, 1% Triton X-100, 20 mM tris-HCl (pH 8.1), 150 mM NaCl, and 2 mM EDTA]. After overnight incubation, beads were washed twice with 1 ml of 2% SDS, twice with 1 ml of radioimmunoprecipitation assay (RIPA) buffer containing 0.5 M NaCl, twice with 1 ml of LiCl buffer [250 mM LiCl, 0.5% NP-40, 0.5% sodium deoxycholate, 1 mM EDTA, and 10 mM tris-HCl (pH 8.0)], and twice with 1 ml of TE buffer [10 mM tris-HCl and 1 mM EDTA (pH 8.0)]. Beads

were then incubated with 300 μ l of SDS elution buffer [1% SDS, 10 mM EDTA, and 50 mM tris-HCl (pH 8.0)] at 65°C overnight with shaking at 1000 rpm to elute bound chromatin and reverse cross-linking. Eluted chromatin was transferred to new tubes and treated with 3 μ l of ribonuclease A (RNase A) (5 mg/ml) for 30 min, followed by treatment with 3 μ l of proteinase K (20 mg/ml; Invitrogen) at 37°C for 2 hours and purification using QIAquick spin columns (QIAGEN). One to 10 ng of ChIP DNA was processed for library generation using the NEBNext Ultra II ChIP sequencing (ChIP-seq) Library Prep kit (NEB) following the manufacturer's protocol. Libraries were pooled and sequenced on an Illumina NextSeq 500 system.

LAMPS-ChIP-seq data analysis

ChIP-seq raw reads were trimmed using Cutadapt (55) with the parameters $-q$ 20 and $-m$ 10 and aligned to the hg38 human genome assembly using Bowtie2 (56) with parameter $-k$ 1. Peak calling was performed using MACS (57) using the $--nomodel$ parameter. Peaks that overlapped with the blacklist regions annotated by the ENCODE project (58), the repeat masked region (chr3:93,469,828 to 93,471,328 and chr16:34,571,939 to 34,576,439; hg38), or the validated nontargeting sgRNA enriched regions (chr16:34,580,740 to 34,583,740; hg38) were removed. To compare the ChIP-seq intensities in samples prepared from cells expressing the target-specific sgRNAs versus the no sgRNA control, MANorm (59) was applied to remove systematic bias between samples and to calculate the normalized ChIP-seq read densities of each peak for all samples. The window size was 1500 bp, which matched the average width of the identified ChIP-seq peaks.

LAMPS-ChIP-qPCR

A total of 0.5×10^7 to 1×10^7 LAMPS-expressing HeLa stable cells transduced with sgHS2 were used. The captured DNA was isolated following the LAMPS-ChIP-seq protocol described above and analyzed by qPCR. For 5% input control samples, 80 μ l of SDS elution buffer was added directly to 20 μ l of sheared chromatin before IP. The samples were incubated at 65°C overnight to reverse cross-linking. DNA fragments were purified using the QIAGEN QIAquick PCR Purification Kit and eluted with 50 μ l of elution buffer (EB). Primer sequences are listed in table S3.

LAMPS-3C-seq

Library preparation and sequencing

A total of 1×10^7 to 5×10^7 cells were harvested and washed twice with $1 \times$ PBS and cross-linked with 1% formaldehyde for 10 min at room temperature with gentle rocking. The cross-linking reaction was quenched by 0.125 M glycine for 5 min at room temperature, followed by two washes with $1 \times$ PBS. Cross-linked cells were resuspended in 1 ml of ice-cold cell lysis buffer [25 mM tris-HCl (pH 7.4), 85 mM KCl, and 0.1% Triton X-100] freshly supplemented with 1 mM DTT and 1:100 protease inhibitor cocktail and rotated for 30 min at 4°C. Cell lysates were centrifuged at 2300g for 5 min at 4°C to isolate nuclei. Nuclei were washed with 500 μ l of ice-cold $1 \times$ Dpn II digestion buffer (NEB), resuspended in 100 μ l of 0.5% SDS, and incubated for 10 min at 62°C. SDS was sequestered by adding 60 μ l of 10% Triton X-100 (final concentration of 1.67%) and 376 μ l of double distilled water (ddH₂O), followed by incubation at 37°C for 30 min. Nuclei were digested using 300 U of Dpn II (NEB) with 60 μ l of 10X Dpn II buffer with rotation overnight at 37°C. Dpn II was inactivated at 62°C for 20 min and immediately cooled on ice. The digested nuclei were diluted with 2.4 ml of $1.15 \times$ T4 ligation buffer

(300 μ l of 10 \times NEB T4 ligase buffer and 1.8 ml of ddH₂O, freshly supplemented with 1:100 proteinase inhibitor cocktail). Chromatin was proximity ligated by adding 15 μ l of NEB T4 DNA ligase (400 U/ μ l) with rotation at 16°C overnight, followed by rotation for 30 min at room temperature the next morning. Nuclei were collected by centrifugation at 2300g for 5 min at 4°C and resuspended in 500 μ l of RIPA 0 buffer [0.1% SDS, 1% Triton X-100, 1 mM EDTA, 10 mM tris-HCl (pH 7.4), and 0.1% sodium deoxycholate (NaDOC)] supplemented with 0.25% sarkosyl (Sigma-Aldrich), followed by sonication to shear chromatin to an average size of \sim 500 bp using a Branson Sonifier 450 ultrasonic processor (10% output, 0.5-s on/1.0-s off for 45 s in ON total or 90 pulses). Sheared chromatin was centrifuged at 16,100g for 10 min at 4°C, and the supernatant was transferred to 1.5 ml of DNA Lo-Bind Eppendorf tubes, and a final concentration of 300 mM NaCl was added. Twenty microliters of the MyOne Streptavidin Dynabeads MyOne T1 per sample were prewashed with ChIP dilution buffer and added to sheared chromatin for binding overnight at 4°C with rotation. After overnight incubation, beads were washed twice with 1 ml of 2% SDS, twice with 1 ml of high-salt wash buffer [0.1% NaDOC, 1% Triton X-100, 1 mM EDTA, 50 mM HEPES (pH 7.5), and 500 mM NaCl], twice with 1 ml of LiCl wash buffer [250 mM LiCl, 0.5% NP-40, 0.5% NaDOC, 1 mM EDTA, and 10 mM tris-HCl (pH 8.1)], and twice with 1 ml of TE buffer. The chromatin was resuspended in SDS elution buffer [1% SDS, 10 mM EDTA, and 50 mM tris-HCl (pH 8.0)] followed by reverse cross-linking and proteinase K digestion at 65°C overnight. Eluted DNA was removed from beads and purified using QIAquick spin columns (QIAGEN). Two to 5 ng of 3C DNA was processed for library generation using the NEBNext Ultra II DNA Library Prep kit (NEB). Libraries were pooled and paired-end sequencing was performed on an Illumina NextSeq 500 system.

LAMPS-3C-seq data analysis

Raw reads were processed as previously described (21, 22). Briefly, read pairs of replicate experiments were merged and mapped separately to human (hg38) genome assembly. Unmapped reads were searched for Dpn II cut sites and in silico digested, and each digested pair was remapped to hg38. The mapped reads from both procedures were merged, and reads with low mapping quality were removed. Uniquely mapped reads were paired and PCR duplicates were removed. For each sgRNA-targeted region, the preprocessed read pairs were used to define its peak size. For each peak region, read pairs with both ends within the same peak region were considered as self-ligations and removed before downstream analysis. Read pairs with only one end within the peak region were considered as paired-end tags for analyzing long-range chromatin interactions.

LAMPS-proteomics

Biotinylated dCas9-mediated affinity purification

A total of 5×10^7 dCas9-CRY2^{Clust}-FUS^N (or FUS^{Nmut}) expressing HeLa stable cells transduced with sgHS2 was harvested, cross-linked with 1% formaldehyde for 10 min with gentle rocking, and quenched with 0.125 M of glycine for 5 min at room temperature. Cells were washed twice with 1 \times PBS, lysed with 1 ml of ice-cold cell lysis buffer [25 mM tris-HCl, 85 mM KCl, 0.1% and Triton X-100 (pH 7.4)] freshly supplemented with 1 mM DTT and 1:100 protease inhibitor cocktail (APEX-BIO), and rotated for 1 hour at 4°C. Cell lysates were centrifuged at 2500g for 5 min at 4°C to isolate nuclei, and a second wash with 1 ml of ice-cold cell lysis buffer

was performed. Washed nuclei were gently resuspended in 0.4 ml of 4% SDS nuclear lysis buffer [50 mM tris-HCl (pH 7.4), 1 mM EDTA, and 0.5% SDS] freshly supplemented with 1 mM DTT and 1:100 protease inhibitor cocktail and incubated for 10 min at room temperature. Nuclei were further resuspended with 1.2 ml of urea buffer [8 M urea, 1 mM EDTA (pH 8.0), and 100 mM ammonium bicarbonate] by pipetting until homogenous (use low-binding pipette tips to reduce material loss). Lysed nuclei were spun at 16,000g for 15 min at a fixed 22°C (temperature-regulated ultracentrifuge). Chromatin pellets were washed once with 1.6 ml of 4% SDS nuclear lysis buffer to wash out urea, spun again, and then washed twice with 1 ml of 10 mM KCl cell lysis buffer to wash out SDS (same as above but with 10 mM KCl to avoid SDS precipitation). Washed chromatin were resuspended into 0.8 ml of RIPA 0 buffer [10 mM tris-HCl (pH 7.4), 1 mM EDTA (pH 8.0), 0.1% SDS, 1% Triton X-100, and 0.1% NaDOC] and sonicated to shear chromatin to an average size of 300 to 600 bp using a Branson Sonifier 450 ultrasonic processor (10% amplitude, 0.5-s on/1-s off for 30 s in ON total or 60 pulses). Sheared chromatin was centrifuged at 16,100g for 10 min at 4°C. The clarified supernatant was transferred to new tubes and 150 mM final NaCl was added. Fifty microliters of the Streptavidin Dynabeads MyOne T1 (Thermo Fischer Scientific, #65602 or Invitrogen, #656-01) per sample was prewashed three times in 1 ml of RIPA 0.3 buffer [10 mM tris-HCl (pH 7.4), 1 mM EDTA (pH 8.0), 0.1% SDS, 1% Triton X-100, 0.1% NaDOC, and 300 mM NaCl], and beads were added to the soluble chromatin and rotated overnight at 4°C. After overnight incubation, streptavidin beads were washed 10 times with 1 ml of ice-cold RIPA wash buffer (containing 0.5 M LiCl) at 4°C, once with 1 ml of ice-cold 1 \times PBS, and twice with 1 ml of freshly made 100 mM ammonium bicarbonate solution at 4°C. After the ammonium bicarbonate wash, the samples were transferred to new Protein Lo-Bind Eppendorf tubes. The beads for proteomics were quickly spun and placed onto a magnetic rack to completely remove residual wash buffer.

In-solution digestion and peptide isolation

To improve the sensitivity and minimize sample loss associated with in-gel digestion, we performed in-solution on-bead trypsin digestion. Briefly, the washed streptavidin beads were resuspended in 10 μ l of sequencing grade modified trypsin (10 ng/ μ l; Promega, catalog no. V5111) in 100 mM ammonium bicarbonate (Sigma-Aldrich), and the beads-trypsin mix was incubated at 37°C with shaking at 1000 rpm for 30 min followed by overnight incubation at 37°C without shaking. An additional 10 μ l of trypsin (10 ng/ μ l) was added the next morning and incubated for another 4 hours at 37°C. After a second round of digestion, the beads were isolated and the clear supernatant containing digested peptides were transferred to a new 1.5 ml of Protein Lo-Bind Eppendorf tube. One hundred percent of formic acid (Thermo Fisher Scientific, #A117-50) was added to the solution to a 5% final concentration. The peptide solution was submitted to the UT Southwestern Proteomics Core for mass spectrometry analysis.

Proteomics data analysis

The liquid chromatography–tandem mass spectrometry data were analyzed using Proteome Discoverer 2.4 with the “matched between runs” parameter and searched against the UniProt human protein database to assign peptides to master proteins. We used the DEP package from Bioconductor (www.bioconductor.org/packages/release/bioc/vignettes/DEP/inst/doc/DEP.html) to normalize the protein intensities, impute missing values, and calculate

the fold changes between samples. From three biological replicate samples for both dark control samples and light-illuminated samples, 258 and 184 nuclear proteins showed significant enrichment or depletion (\log_2 fold change ≥ 1 or ≤ -1 , $P < 0.01$) in LAMPS-induced condensates (light) relative to the dark controls.

ChIP-qPCR

A total of 0.5×10^7 to 1×10^7 LAMPS-expressing HeLa stable cells transduced with sgHS2s were used for each ChIP experiment. The sheared chromatin was prepared following the ChIP-seq protocol described above and incubated with RAD21 (Abcam, #ab992), SMC1 (Bethyl Laboratories, #A300-055A) and RNA Pol II subunit RBP1 (BioLegend, #664912) antibodies overnight at 4°C, respectively. Protein A Dynabeads (Invitrogen, #10001D) were pre-washed twice with ChIP dilution buffer [0.1% SDS, 1% Triton X-100, 20 mM tris-HCl (pH 8.1), 150 mM NaCl, and 2 mM EDTA] and added to each ChIP sample, followed by incubation for 3 to 4 hours at 4°C. Beads were washed twice with 1 ml of RIPA 0 buffer, twice with 1 ml of RIPA 0.3 buffer [0.1% SDS, 1% Triton X-100, 10 mM tris-HCl (pH 7.4), 1 mM EDTA (pH 8.0), 0.1% NaDOC, and 0.3 M NaCl], twice with 1 ml of LiCl buffer [250 mM LiCl, 0.5% NP-40, 0.5% sodium deoxycholate, 1 mM EDTA, and 10 mM tris-HCl (pH 8.0)], and twice with 1 ml of TE buffer [10 mM tris-HCl and 1 mM EDTA (pH 8.0)]. Beads were then incubated with 100 μ l of SDS elution buffer [1% SDS, 10 mM EDTA, and 50 mM tris-HCl (pH 8.0)] at 65°C overnight with shaking at 1000 rpm to elute bound chromatin and reverse cross-linking. For 5% input control samples, 80 μ l of SDS elution buffer was added directly to 20 μ l of sheared chromatin without IP. Eluted chromatin was transferred to new tubes from magnetic beads and treated with 1 μ l of RNase A (5 mg/ml) for 30 min, followed by treatment with 1 μ l of proteinase K (20 mg/ml; Invitrogen) at 37°C for 2 hours, and purified using QIAquick Spin Columns (QIAGEN). One to 10 ng of ChIP DNA was analyzed by qPCR.

Assay for transposase-accessible chromatin using sequencing

A total of 5×10^4 cells were washed twice in $1 \times$ PBS and resuspended in 500 μ l of cell lysis buffer [10 mM tris-HCl (pH 7.4), 10 mM NaCl, 3 mM MgCl₂, and 0.1% NP-40]. Cell lysates were centrifuged at 500g for 10 min at 4°C. Isolated nuclei were resuspended in 50 μ l of tagmentation mix [10 mM TAPS {[tris(hydroxymethyl)methylamino]propanesulfonic acid} (pH 8.0) (Sigma-Aldrich), 5 mM MgCl₂, and 2.5 μ l of Tn5 transposase] and incubated at 37°C for 30 min. Tagmentation reaction was quenched by adding 10 μ l of 0.2% SDS followed by incubation at room temperature for 2 min and 55°C for 7 min. Tn5 transposase-tagged DNA was purified using the QIAquick MinElute PCR Purification kit (QIAGEN), amplified using the KAPA HiFi Hotstart PCR Kit (KAPA), and sequenced on an Illumina NextSeq 500 system. ATAC-seq raw reads were trimmed to remove the adaptor sequence using Cutadapt (55) and aligned to hg38 genome assembly using Bowtie1 (60) with the parameters --best --strata -k 1 -m 1. Only tags that uniquely mapped to the genome were used for analysis.

Statistics and reproducibility

Statistical details including N , mean, and statistical significance values are indicated in the text and figure legends. Error bars in the experiments represent SEM or SD from either independent

experiments or independent samples. All statistical analyses were performed using GraphPad Prism, and the detailed information about statistical methods is specified in figure legends or Materials and Methods. The numbers of independent experiments or biological replicate samples and P values ($*P < 0.05$, $**P < 0.01$, $***P < 0.001$, and $****P < 0.0001$; n.s., not significant) are provided in individual figures. $P < 0.05$ was considered statistically significant.

Supplementary Materials

This PDF file includes:

Figs. S1 to S6

Legends for tables S1 to S4

Other Supplementary Material for this manuscript includes the following:

Tables S1 to S4

[View/request a protocol for this paper from Bio-protocol.](#)

REFERENCES AND NOTES

- S. F. Banani, H. O. Lee, A. A. Hyman, M. K. Rosen, Biomolecular condensates: Organizers of cellular biochemistry. *Nat. Rev. Mol. Cell Biol.* **18**, 285–298 (2017).
- A. A. Hyman, C. A. Weber, F. Julicher, Liquid-liquid phase separation in biology. *Ann. Rev. Cell Dev. Biol.* **30**, 39–58 (2014).
- D. L. J. Lafontaine, J. A. Riback, R. Bascetin, C. P. Brangwynne, The nucleolus as a multiphase liquid condensate. *Nat. Rev. Mol. Cell Biol.* **22**, 165–182 (2021).
- B. R. Sabari, A. Dall'Agnese, R. A. Young, Biomolecular condensates in the nucleus. *Trends Biochem. Sci.* **45**, 961–977 (2020).
- A. Molliex, J. Temirov, J. Lee, M. Coughlin, A. P. Kanagaraj, H. J. Kim, T. Mittag, J. P. Taylor, Phase separation by low complexity domains promotes stress granule assembly and drives pathological fibrillization. *Cell* **163**, 123–133 (2015).
- A. C. Murthy, G. L. Dignon, Y. Kan, G. H. Zerze, S. H. Parekh, J. Mittal, N. L. Fawzi, Molecular interactions underlying liquid-liquid phase separation of the FUS low-complexity domain. *Nat. Struct. Mol. Biol.* **26**, 637–648 (2019).
- J. C. Schwartz, T. R. Cech, R. R. Parker, Biochemical properties and biological functions of FET proteins. *Annu. Rev. Biochem.* **84**, 355–379 (2015).
- T. Ukmar-Godec, S. Hutten, M. P. Grieshop, N. Rezaei-Ghaleh, M.-S. Cima-Omori, J. Biernat, E. Mandelkow, J. Söding, D. Dormann, M. Zweckstetter, Lysine/RNA-interactions drive and regulate biomolecular condensation. *Nat. Commun.* **10**, 2909 (2019).
- A. Boija, I. A. Klein, B. R. Sabari, A. Dall'Agnese, E. L. Coffey, A. V. Zamudio, C. H. Li, K. Shrinivas, J. C. Manteiga, N. M. Hannett, B. J. Abraham, L. K. Afeyan, Y. E. Guo, J. K. Rimel, C. B. Fant, J. Schuijers, T. I. Lee, D. J. Taatjes, R. A. Young, Transcription factors activate genes through the phase-separation capacity of their activation domains. *Cell* **175**, 1842–1855.e16 (2018).
- W.-K. Cho, J.-H. Spille, M. Hecht, C. Lee, C. Li, V. Grube, I. I. Cisse, Mediator and RNA polymerase II clusters associate in transcription-dependent condensates. *Science* **361**, 412–415 (2018).
- S. Chong, C. Dugast-Darzacq, Z. Liu, P. Dong, G. M. Dailey, C. Cattoglio, A. Heckert, S. Banala, L. Lavis, X. Darzacq, R. Tjian, Imaging dynamic and selective low-complexity domain interactions that control gene transcription. *Science* **361**, eaar2555 (2018).
- B. R. Sabari, A. Dall'Agnese, A. Boija, I. A. Klein, E. L. Coffey, K. Shrinivas, B. J. Abraham, N. M. Hannett, A. V. Zamudio, J. C. Manteiga, C. H. Li, Y. E. Guo, D. S. Day, J. Schuijers, E. Vasile, S. Malik, D. Hnisz, T. I. Lee, I. I. Cisse, R. G. Roeder, P. A. Sharp, A. K. Chakraborty, R. A. Young, Coactivator condensation at super-enhancers links phase separation and gene control. *Science* **361**, eaar3958 (2018).
- W. A. Whyte, D. A. Orlando, D. Hnisz, B. J. Abraham, C. Y. Lin, M. H. Kagey, P. B. Rahl, T. I. Lee, R. A. Young, Master transcription factors and mediator establish super-enhancers at key cell identity genes. *Cell* **153**, 307–319 (2013).
- Y. Shin, J. Berry, N. Pannucci, M. P. Haataja, J. E. Toettcher, C. P. Brangwynne, Spatiotemporal control of intracellular phase transitions using light-activated optoDroplets. *Cell* **168**, 159–171.e14 (2017).
- D. Bracha, M. T. Walls, M.-T. Wei, L. Zhu, M. Kurian, J. L. Avalos, J. E. Toettcher, C. P. Brangwynne, Mapping local and global liquid phase behavior in living cells using photo-oligomerizable seeds. *Cell* **175**, 1467–1480.e13 (2018).

16. E. Dine, A. A. Gil, G. Uribe, C. P. Brangwynne, J. E. Toettcher, Protein phase separation provides long-term memory of transient spatial stimuli. *Cell Syst.* **6**, 655–663.e5 (2018).
17. Y. Shin, Y.-C. Chang, D. S. W. Lee, J. Berry, D. W. Sanders, P. Ronceray, N. S. Wingreen, M. Haataja, C. P. Brangwynne, Liquid nuclear condensates mechanically sense and restructure the genome. *Cell* **175**, 1481–1491.e13 (2018).
18. N. Schneider, F.-G. Wieland, D. Kong, A. A. M. Fischer, M. Hörner, J. Timmer, H. Ye, W. Weber, Liquid-liquid phase separation of light-inducible transcription factors increases transcription activation in mammalian cells and mice. *Sci. Adv.* **7**, eabd3568 (2021).
19. P. Más, P. F. Devlin, S. Panda, S. A. Kay, Functional interaction of phytochrome B and cryptochrome 2. *Nature* **408**, 207–211 (2000).
20. Y. Shin, C. P. Brangwynne, Liquid phase condensation in cell physiology and disease. *Science* **357**, eaaf4382 (2017).
21. X. Liu, Y. Zhang, Y. Chen, M. Li, F. Zhou, K. Li, H. Cao, M. Ni, Y. Liu, Z. Gu, K. E. Dickerson, S. Xie, G. C. Hon, Z. Xuan, M. Q. Zhang, Z. Shao, J. Xu, In situ capture of chromatin interactions by biotinylated dCas9. *Cell* **170**, 1028–1043.e19 (2017).
22. X. Liu, Y. Chen, Y. Zhang, Y. Liu, N. Liu, G. A. Botten, H. Cao, S. H. Orkin, M. Q. Zhang, J. Xu, Multiplexed capture of spatial configuration and temporal dynamics of locus-specific 3D chromatin by biotinylated dCas9. *Genome Biol.* **21**, 59 (2020).
23. J. Dekker, K. Rippe, M. Dekker, N. Kleckner, Capturing chromosome conformation. *Science* **295**, 1306–1311 (2002).
24. X. Liu, Y. Zhang, Y. Chen, M. Li, Z. Shao, M. Q. Zhang, J. Xu, CAPTURE: In situ analysis of chromatin composition of endogenous genomic loci by biotinylated dCas9. *Curr. Protoc. Mol. Biol.* **123**, e64 (2018).
25. A. Taslimi, J. D. Vrana, D. Chen, S. Borinskaya, B. J. Mayer, M. J. Kennedy, C. L. Tucker, An optimized optogenetic clustering tool for probing protein interaction and function. *Nat. Commun.* **5**, 4925 (2014).
26. L. Duan, J. Hope, Q. Ong, H.-Y. Lou, N. Kim, C. M. Carthy, V. Acero, M. Z. Lin, B. Cui, Understanding CRY2 interactions for optical control of intracellular signaling. *Nat. Commun.* **8**, 547 (2017).
27. H. Park, N. Y. Kim, S. Lee, N. Kim, J. Kim, W. D. Heo, Optogenetic protein clustering through fluorescent protein tagging and extension of CRY2. *Nat. Commun.* **8**, 30 (2017).
28. V. G. Sankaran, J. Xu, T. Ragoczy, G. C. Ippolito, C. R. Walkley, S. D. Maika, Y. Fujiwara, M. Ito, M. Groudine, M. A. Bender, P. W. Tucker, S. H. Orkin, Developmental and species-divergent globin switching are driven by BCL11A. *Nature* **460**, 1093–1097 (2009).
29. S. F. Shimobayashi, P. Ronceray, D. W. Sanders, M. P. Haataja, C. P. Brangwynne, Nucleation landscape of biomolecular condensates. *Nature* **599**, 503–506 (2021).
30. Y. E. Guo, J. C. Manteiga, J. E. Henninger, B. R. Sabari, A. Dall'Agnese, N. M. Hannett, J.-H. Spille, L. K. Afeyan, A. V. Zamudio, K. Shrinivas, B. J. Abraham, A. Boija, T.-M. Decker, J. K. Rimmel, C. B. Fant, T. I. Lee, I. I. Cisse, P. A. Sharp, D. J. Taatjes, R. A. Young, Pol II phosphorylation regulates a switch between transcriptional and splicing condensates. *Nature* **572**, 543–548 (2019).
31. J. E. Henninger, O. Oksuz, K. Shrinivas, I. Sagi, G. L. Roy, M. M. Zheng, J. O. Andrews, A. V. Zamudio, C. Lazaris, N. M. Hannett, T. I. Lee, P. A. Sharp, I. I. Cissé, A. K. Chakraborty, R. A. Young, RNA-mediated feedback control of transcriptional condensates. *Cell* **184**, 207–225.e24 (2021).
32. W. Deng, J. Lee, H. Wang, J. Miller, A. Reik, P. D. Gregory, A. Dean, G. A. Blobel, Controlling long-range genomic interactions at a native locus by targeted tethering of a looping factor. *Cell* **149**, 1233–1244 (2012).
33. P. Huang, C. A. Keller, B. Giardine, J. D. Grevet, J. O. J. Davies, J. R. Hughes, R. Kurita, Y. Nakamura, R. C. Hardison, G. A. Blobel, Comparative analysis of three-dimensional chromosomal architecture identifies a novel fetal hemoglobin regulatory element. *Genes Dev.* **31**, 1704–1713 (2017).
34. M. S. Ivaldi, L. F. Diaz, L. Chakalova, J. Lee, I. Krivega, A. Dean, Fetal γ -globin genes are regulated by the *BGLT3* long noncoding RNA locus. *Blood* **132**, 1963–1973 (2018).
35. T. Masuda, X. Wang, M. Maeda, M. C. Canver, F. Sher, A. P. W. Funnell, C. Fisher, M. Suci, G. E. Martyn, L. J. Norton, C. Zhu, R. Kurita, Y. Nakamura, J. Xu, D. R. Higgs, M. Crossley, D. E. Bauer, S. H. Orkin, P. V. Kharchenko, T. Maeda, Transcription factors LRF and BCL11A independently repress expression of fetal hemoglobin. *Science* **351**, 285–289 (2016).
36. Y. Shen, J. M. Verboon, Y. Zhang, N. Liu, Y. J. Kim, S. Marglous, S. K. Nandakumar, R. A. Voit, C. Fiorini, A. Ejaz, A. Basak, S. H. Orkin, J. Xu, V. G. Sankaran, A unified model of human hemoglobin switching through single-cell genome editing. *Nat. Commun.* **12**, 4991 (2021).
37. I. A. Tchasovnikarova, R. T. Timms, N. J. Matheson, K. Wals, R. Antrobus, B. Göttgens, G. Dougan, M. A. Dawson, P. J. Lehner, Epigenetic silencing by the HUSH complex mediates position-effect variegation in human cells. *Science* **348**, 1481–1485 (2015).
38. Z. Gu, Y. Liu, Y. Zhang, H. Cao, J. Lyu, X. Wang, A. Wylie, S. J. Newkirk, A. E. Jones, M. Lee Jr, G. A. Botten, M. Deng, K. E. Dickerson, C. C. Zhang, W. An, J. M. Abrams, J. Xu, Silencing of LINE-1 retrotransposons is a selective dependency of myeloid leukemia. *Nat. Genet.* **53**, 672–682 (2021).
39. H. Lyons, R. T. Veettil, P. Pradhan, C. Fornero, N. De La Cruz, K. Ito, M. Eppert, R. G. Roeder, B. R. Sabari, Functional partitioning of transcriptional regulators by patterned charge blocks. *Cell* **186**, 327–345.e28 (2023).
40. R. G. Roeder, 50+ years of eukaryotic transcription: An expanding universe of factors and mechanisms. *Nat. Struct. Mol. Biol.* **26**, 783–791 (2019).
41. D. Hnisz, K. Shrinivas, R. A. Young, A. K. Chakraborty, P. A. Sharp, A phase separation model for transcriptional control. *Cell* **169**, 13–23 (2017).
42. M.-T. Wei, Y.-C. Chang, S. F. Shimobayashi, Y. Shin, A. R. Strom, C. P. Brangwynne, Nucleated transcriptional condensates amplify gene expression. *Nat. Cell Biol.* **22**, 1187–1196 (2020).
43. J. Trojanowski, L. Frank, A. Rademacher, N. Mücke, P. Grigaitis, K. Rippe, Transcription activation is enhanced by multivalent interactions independent of phase separation. *Mol. Cell* **82**, 1878–1893.e10 (2022).
44. S. Chong, T. G. W. Graham, C. Dugast-Darzacq, G. M. Dailey, X. Darzacq, R. Tjian, Tuning levels of low-complexity domain interactions to modulate endogenous oncogenic transcription. *Mol. Cell* **82**, 2084–2097.e5 (2022).
45. L. J. Bugaj, A. T. Choksi, C. K. Mesuda, R. S. Kane, D. V. Schaffer, Optogenetic protein clustering and signaling activation in mammalian cells. *Nat. Methods* **10**, 249–252 (2013).
46. J. H. Ahn, E. S. Davis, T. A. Daugird, S. Zhao, I. Y. Quiroga, H. Uryu, J. Li, A. J. Storey, Y.-H. Tsai, D. P. Keeley, S. G. Mackintosh, R. D. Edmondson, S. D. Byrum, L. Cai, A. J. Tackett, D. Zheng, W. R. Legant, D. H. Phanstiel, G. G. Wang, Phase separation drives aberrant chromatin looping and cancer development. *Nature* **595**, 591–595 (2021).
47. L. Li, H. Liu, P. Dong, D. Li, W. R. Legant, J. B. Grimm, L. D. Lavis, E. Betzig, R. Tjian, Z. Liu, Real-time imaging of Huntingtin aggregates diverting target search and gene transcription. *eLife* **5**, e17056 (2016).
48. M. V. Staller, E. Ramirez, S. R. Kotha, A. S. Holehouse, R. V. Pappu, B. A. Cohen, Directed mutational scanning reveals a balance between acidic and hydrophobic residues in strong human activation domains. *Cell Syst.* **13**, 334–345.e5 (2022).
49. T. Fukaya, B. Lim, M. Levine, Enhancer control of transcriptional bursting. *Cell* **166**, 358–368 (2016).
50. M. Garcia-Jove Navarro, S. Kashida, R. Chouaib, S. Souquere, G. Pierron, D. Weil, Z. Gueroui, RNA is a critical element for the sizing and the composition of phase-separated RNA-protein condensates. *Nat. Commun.* **10**, 3230 (2019).
51. C. Roden, A. S. Gladfelter, RNA contributions to the form and function of biomolecular condensates. *Nat. Rev. Mol. Cell Biol.* **22**, 183–195 (2021).
52. G. Ma, L. He, S. Liu, J. Xie, Z. Huang, J. Jing, Y.T. Lee, R. Wang, H. Luo, W. Han, Y. Huang, Y. Zhou, Optogenetic engineering to probe the molecular choreography of STIM1-mediated cell signaling. *Nat. Commun.* **11**, 1039 (2020).
53. X. Han, D. Yu, R. Gu, Y. Jia, Q. Wang, A. Jaganathan, X. Yang, M. Yu, N. Babault, C. Zhao, H. Yi, Q. Zhang, M.-M. Zhou, L. Zeng, Roles of the BRD4 short isoform in phase separation and active gene transcription. *Nat. Struct. Mol. Biol.* **27**, 333–341 (2020).
54. J. Huang, X. Liu, D. Li, Z. Shao, H. Cao, Y. Zhang, E. Trompouki, T. V. Bowman, L. I. Zon, G.-C. Yuan, S. H. Orkin, J. Xu, Dynamic control of enhancer repertoires drives lineage and stage-specific transcription during hematopoiesis. *Dev. Cell* **36**, 9–23 (2016).
55. M. Martin, Cntadappt removes adapter sequences from high-throughput sequencing reads. *17*, 3 (2011).
56. B. Langmead, S. L. Salzberg, Fast gapped-read alignment with Bowtie 2. *Nat. Methods* **9**, 357–359 (2012).
57. Y. Zhang, T. Liu, C. A. Meyer, J. Eeckhoutte, D. S. Johnson, B. E. Bernstein, C. Nusbaum, R. M. Myers, M. Brown, W. Li, X. S. Liu, Model-based analysis of ChIP-Seq (MACS). *Genome Biol.* **9**, R137 (2008).
58. E. P. Consortium, An integrated encyclopedia of DNA elements in the human genome. *Nature* **489**, 57–74 (2012).
59. Z. Shao, Y. Zhang, G. C. Yuan, S. H. Orkin, D. J. Waxman, MAnorm: A robust model for quantitative comparison of ChIP-Seq data sets. *Genome Biol.* **13**, R16 (2012).
60. B. Langmead, C. Trapnell, M. Pop, S. L. Salzberg, Ultrafast and memory-efficient alignment of short DNA sequences to the human genome. *Genome Biol.* **10**, R25 (2009).

Acknowledgments: We thank W.-P. Ge and X. Gao for helping with imaging studies, C.-M. Chang for the BRD4 cDNA, and other Xu laboratory members for technical support. We thank the UTSW Quantitative Light Microscopy Core, a Shared Resource of the Harold C. Simmons Cancer Center, supported by P30CA142543, The Nikon SoRa Spinning Disk confocal microscope was purchased with 15100D028630-01. **Funding:** G.A.B. was supported by the American Heart Association predoctoral fellowship (827234). J.T.S. is supported by Cancer Biology T32CA124334 from the Simmons Comprehensive Cancer Center at UTSW. J.X. is a scholar of the Leukemia & Lymphoma Society (LLS) and an American Society of Hematology (ASH) scholar. This work was supported by National Institutes of Health grants R01DK111430, R01CA230631, R01CA259581, and R21AI158240 (to J.X.), as well as R01CA232017 and R01GM144986 (to Y.Zhou); by Cancer Prevention and Research Institute of Texas grants (RP190417 and RP220375 to J.X. and RP210070 to Y.Zhou); and by Welch Foundation grants I-

1942 (to J.X.) and BE-1913-20220331 (to Y.Zhou). **Author contributions:** Conceptualization: Y.J.K., M.L.J., Y.Zhou, and J.X. Methodology: Y.J.K., M.L.J., Y.-T.L., J.J., J.T.S., G.A.B., L.H., J.L., Y.Zhang, Y.Zhou, M.M., and J.X. Investigation: Y.J.K., J.J., M.L.J., Y.-T.L., J.T.S., G.A.B., L.H., J.L., and Y.Zhang. Writing—original draft: Y.J.K., J.J., M.L.J., Y.-T.L., and J.X. Writing—review and editing: Y.J.K., M.L.J., Y.Zhou, and J.X. Funding acquisition: M.M., P.L., Y.Zhou, and J.X. Supervision: Y.Zhou and J.X. **Competing interests:** The authors declare that they have no competing interests. **Data and materials availability:** All raw and processed ATAC-seq, LAMPS–ChIP-seq, and LAMPS–3C-seq data are available in the Gene Expression Omnibus (GEO): GSE180550. The accession

numbers for all genomic datasets are listed in table S4. All data needed to evaluate the conclusions in the paper are present in the paper and/or the Supplementary Materials.

Submitted 2 December 2022

Accepted 28 February 2023

Published 31 March 2023

10.1126/sciadv.adg1123